

THESIS FOR THE DEGREE OF LICENTIATE OF ENGINEERING

---

# Low-Power HEMT LNAs for Quantum Computing

YIN ZENG



**CHALMERS**  
UNIVERSITY OF TECHNOLOGY

Department of Microtechnology and Nanoscience  
Chalmers University of Technology  
Gothenburg, Sweden, 2023

# Low-Power HEMT LNAs for Quantum Computing

YIN ZENG

Copyright © 2023 YIN ZENG  
All rights reserved.

Technical Report No. 462  
ISSN 1652-0769  
This thesis has been prepared using L<sup>A</sup>T<sub>E</sub>X.

Chalmers University of Technology  
Microtechnology and Nanoscience - MC2  
Terahertz and Millimetre Wave Laboratory  
SE-412 96 Gothenburg, Sweden  
Phone: +46 (0)31 772 1000  
[www.chalmers.se](http://www.chalmers.se)

Printed by Chalmers Reproservice  
Gothenburg, Sweden, September, 2023

*'I have no special talents. I am only passionately curious' - Albert Einstein*



## Abstract

The rapid development of quantum computing technology predicts much more qubits to handle in the detection, readout, and amplification of qubits than in today's system. Due to the limited cooling capability of the dilution refrigerator, the current low-noise amplifiers (LNAs) are in need of ten to hundred times reduced dc power consumption yet with lowest noise temperature at qubit readout frequencies, typically 4-12 GHz. Cryogenic indium phosphide (InP) high electron mobility transistor (HEMT) LNAs, are the standard qubit amplifier at 4 K in today's superconducting quantum system. However, the power consumption of current InP HEMT LNAs is still too high for future quantum system up-scaling.

A small-signal noise model of a 100-nm gate-length InP HEMTs has been characterized and extracted at 4 K ambient under low-power bias down to 1  $\mu$ W. The extracted low-power small-signal noise models revealed fast degradation points of drain voltage bias for RF and noise performance.

The design goals of the cryogenic LNA were tailored for a superconducting qubit readout application based on the extracted low-power small-signal noise model of the InP HEMT for optimum noise and power consumption trade-off. A cryogenic InP HEMT hybrid LNA operating in the 4-6 GHz frequency range at 200  $\mu$ W with an average noise temperature of 2.0 K has been designed, fabricated and successfully demonstrated, validating the extracted model and design methodology.

An epitaxially-optimized InP HEMT was modeled with the low-power methodology. The comparison of the small-signal noise model parameters to the standard InP HEMT showed improved transconductance, matching, and noise at the same bias power. The demonstrated three-stage cryogenic 4-6 GHz LNA equipped with an optimized HEMT as the first stage achieved 2.0 K average noise temperature at 100  $\mu$ W dc power dissipation, representing a new state-of-the-art. This licentiate thesis has presented experimental evidence that there is large potential in reducing dc power in the cryogenic InP HEMT LNA for qubit readout which can be important for the planned up-scaling in future quantum computing.

**Keywords:** Cryogenic, quantum computing, qubit, low-power, low-noise amplifier, InP HEMT.



## List of Publications

This thesis is based on the following publications:

[A] **Yin Zeng**, Jörgen Stenarson, Peter Sobis, Niklas Wadefalk, Jan Grahn, “A 100- $\mu$ W 4–6 GHz Cryogenic InP HEMT LNA Achieving an Average Noise Temperature of 2.6 K”. Published in *34th Asia-Pacific Microwave Conference* (pp. 13-15). IEEE, Dec, 2022.

[B] **Yin Zeng**, Jörgen Stenarson, Peter Sobis, Niklas Wadefalk, Jan Grahn, “Sub-mW Cryogenic InP HEMT LNA for Qubit Readout”. Accepted for publication in *IEEE Transactions on Microwave Theory and Techniques*, Aug. 2023.

[C] **Yin Zeng**, Jörgen Stenarson, Peter Sobis, Jan Grahn, “100- $\mu$ W Cryogenic HEMT LNAs for Quantum Computing”. Accepted by *18th European Microwave Integrated Circuits Conference*, Sept. 2023.



---

# Contents

---

<b>Abstract</b>	<b>i</b>
<b>List of Papers</b>	<b>iii</b>
<b>1 Introduction</b>	<b>1</b>
1.1 Low-power HEMT LNAs for quantum computing . . . . .	1
1.2 Cryogenic LNAs . . . . .	3
1.3 Thesis scope and outline . . . . .	4
<b>2 Characterization and modeling of low-power HEMT for LNAs in quantum computing</b>	<b>5</b>
2.1 InP HEMT technology . . . . .	6
2.2 Cryogenic small-signal noise model at low power . . . . .	8
HEMT small-signal model parameters at low power . . . . .	9
HEMT noise model and extraction at low power . . . . .	12
<b>3 Low-power HEMT LNA design for qubit readout</b>	<b>21</b>
3.1 Design analysis for qubit readout . . . . .	22
3.2 Design and implementation of low-power LNA for qubit readout	24
3.3 Measurement results and discussion . . . . .	28

<b>4</b>	<b>A low-power LNA for qubit readout using an optimized InP HEMT</b>	<b>33</b>
4.1	Optimized HEMT technology for low power . . . . .	33
4.2	Comparison of small-signal noise models . . . . .	34
4.3	Measurement results and comparison . . . . .	38
4.4	State-of-the-art comparison . . . . .	40
<b>5</b>	<b>Conclusions and future work</b>	<b>43</b>
5.1	Conclusions . . . . .	43
5.2	Future work . . . . .	44
	<b>Acknowledgements</b>	<b>46</b>
	<b>References</b>	<b>49</b>



# CHAPTER 1

---

## Introduction

---

### 1.1 Low-power HEMT LNAs for quantum computing

The high electron mobility transistor (HEMT) low-noise amplifier (LNA) is one of the crucial components in superconducting quantum computers. The quantum processor relies on microwave components at 4-12 GHz [1]. Since the qubit represents a signal power of typically -120 dBm, microwave amplification of qubits becomes critical. In Fig. 1.1, a schematic of a typical qubit handling is presented. The first stage amplifier is a superconducting Josephson parametric amplifier (JPA) or traveling wave parametric amplifier (TWPA). Parametric amplifiers are quantum-noise limited and dissipates nearly zero dc power at 10 mK ambient temperature [2]. Following the superconducting amplifier, the second stage amplifier is the HEMT LNA at the 4 K stage [3], [4]. After around 10 dB loss of the cable, a room-temperature amplifier is followed, to provide amplification before the digitizer [4], [5].

The HEMT LNA in Fig. 1.1 is the focus of this thesis. When the HEMT LNA is used as the second stage amplifier after the parametric amplifier, a



## 1.2 Cryogenic LNAs

The HEMT LNAs used for qubit readout are direct descendants of cryogenic LNAs developed for radio astronomy. Since the first cryogenic LNA was realized by Dr. Sander Weinreb based on GaAs metal–semiconductor field-effect transistor (MESFET) in 1980 [11], the FET-based cryogenic LNA was quickly adopted to replace the parametric amplifiers used in radio astronomy front end for better gain, linearity, bandwidth, and stability [2]. After Mimura’s HEMT invention [12], the GaAs HEMT was first employed for cryogenic LNA in radioastronomy and satellite communication, owing to the significant noise reduction provided by HEMT’s two-dimensional electron gas (2DEG) [13]. Today, the InP HEMT LNA maintains leadership in noise performance, showcasing a three-stage cascaded LNA with 1.2 K average noise temperature at 5 GHz with 4.2 mW dc power dissipation, which is only 5 times the quantum-noise limit [14].

Studies have been carried out to improve the noise performance of InP HEMTs under low-power bias. By the investigation of InP HEMT channel contents, a 2.9 K average noise temperature has been achieved by a cryogenic 4-8 GHz LNA employing 65 % indium channel InP HEMT with 300  $\mu$ W power consumption at 5 K [15], [16]. In another study, the spacer thickness of the InP HEMT epi-structure was optimized to produce a 4-8 GHz cryogenic LNA with 1.4 K average noise with 6.1 mW power consumption [17].

The standard InP HEMT technology has been challenged by SiGe heterojunction bipolar transistors (HBT) for its potential to be integrated with complementary metal-oxide semiconductor (CMOS) processes and high gain [3], [18]. By investigating the model behavior of SiGe HBT under ultra-low power bias, a 1.8-3.6 GHz cryogenic amplifier based on a commercial foundry process (BiCMOS8HP) demonstrated 5 K average noise temperature at 290  $\mu$ W dc power consumption [19]. Furthermore, the cryogenic noise performance of SiGe HBTs was optimized by altering the Ge doping profile to reach lower noise and better matching quality that produced a 4-8 GHz cryogenic LNA with 3.2 K average noise temperature at 1 mW power consumption [20]. Recently, a reconfigurable SiGe HBTs cryogenic LNA has been reported to achieve 4.3 K average noise from 3 to 6 GHz with a tunable bandwidth and 1.8 mW dc power consumption [21]. Despite the significant performance improvements, the SiGe HBT cryogenic LNAs do not surpass InP HEMT technology in terms of noise and low-power performance, in part limited by the generation of shot

noise in the reverse-biased base-collector junction of the HBT.

As an alternative to semiconductor-based cryogenic LNAs for qubit readout, a TWPA was recently proposed to be operated at 4 K [22]. The TWPA demonstrated 1.9 K average noise temperature from 3.5 to 5.5 GHz with 100  $\mu$ W power consumption. However, due to limited dynamic range, low gain, and high cost of the TWPA, the InP HEMT cryogenic LNA is still the preferred choice for qubit readout at 4 K.

### **1.3 Thesis scope and outline**

As mentioned above, future massive up-scaling in quantum computing calls for HEMT LNAs at 4 K with much less dc power than today and still with excellent noise performance. When operating with power levels much below 1 mW, semiconductor-based cryogenic LNAs with a noise temperature below 2.0 K for qubit readout is yet to be realized. This thesis claims that extremely low-power HEMT LNAs can be engineered with much smaller dc power consumption than found in today's quantum readout circuits. The trade-off between noise performance, bandwidth, and power consumption in the InP HEMT has been tailored to meet the superconducting qubit readout requirements.

In Chapter 2 of the thesis, a small-signal noise model of InP HEMT down to 1  $\mu$ W is outlined to determine the best bias strategy for noise and performance trade-off in cryogenic LNA design [Paper A and B]. A two-bias strategy is described for noise extraction at low power. In Chapter 3, the requirements for qubit readout application with respect to the cryogenic HEMT LNAs are discussed and analyzed with the extracted model from Chapter 2 [Paper B]. Furthermore, Chapter 3 presents the design, fabrication, and measurement of a new state-of-art cryogenic HEMT LNA for qubit readout [Paper B]. In Chapter 4, an epitaxially optimized InP HEMT in the LNA is tested. It is found that the optimized HEMT has a large influence on the cryogenic HEMT LNA low-power performance [Paper C]. Finally, the results from this licenciate thesis are concluded in Chapter 5. Future research work to advance HEMT LNAs in superconducting quantum computing is proposed.

## CHAPTER 2

---

### Characterization and modeling of low-power HEMT for LNAs in quantum computing

---

Accurate modeling of small-signal and noise characteristics is crucial for designing RF circuits at low-power conditions. For cryogenic LNA design, the model extraction relies on experimental data measured at 4 K, which is often unavailable for transistor models. Scalable small-signal noise models at cryogenic temperature have been developed for the InP HEMT down to 5 mW/mm [23], [24]. However, this level is not sufficient for designing cryogenic LNA with a total dc power consumption much less than 1 mW.

To fully utilize the RF and noise performance of the transistor in a cryogenic LNA designed for very low power, this chapter presents an investigation of a cryogenic model for InP HEMTs down to 1  $\mu$ W. The developed cryogenic small-signal noise model paves the way for the realization of LNAs requested for future large-scale quantum computing systems.

## 2.1 InP HEMT technology

The transistor used for the model extraction and circuit design was a 100-nm gate-length and  $4 \times 50 \mu\text{m}$  gate-width InP HEMT [25]. This transistor size is well-known to yield sufficient dc and RF device performance for cryogenic LNA designs in today's qubit readout circuits [26]. The epitaxial layer structure from top to bottom was 20 nm InGaAs cap followed by 3 nm InP etch stopper, 8 nm InAlAs barrier, silicon  $\delta$ -doping ( $5 \times 10^{12} \text{ cm}^{-2}$ ), 3 nm InAlAs spacer, 15 nm InGaAs channel with 65% indium content and 500 nm InAlAs buffer layer. The channel electron mobility and sheet carrier concentration was  $12000 \text{ cm}^2/\text{Vs}$  and  $3.6 \times 10^{12} \text{ cm}^{-2}$ , respectively.

The dc characterization was performed at 4 K environment in a Lakeshore model CRX-4K cryogenic probe station. In Fig. 2.1 (a), the drain current  $I_d$  versus drain-source voltage  $V_{ds}$  showed a peak drain current of 900 mA/mm at  $V_{ds} = 0.5 \text{ V}$  with an on-resistance  $R_{on}$  of  $0.33 \Omega \cdot \text{mm}$ . The transfer characteristic of the InP HEMT is plotted in Fig. 2.1 (b). The threshold gate-source voltage  $V_{gs}$  for the device was  $-0.25 \text{ V}$  and the maximum extrinsic transconductance  $g_{m,o}$  reached  $1.8 \text{ S/mm}$  at  $V_{ds} = 0.7 \text{ V}$ .

The magnitude of gate current  $I_g$  presented in Fig. 2.1 (c) was in the order of  $0.1 \mu\text{A/mm}$  for  $V_{ds}$  up to  $0.7 \text{ V}$ , indicating satisfactory control of the gate leakage path [25], [27]. An elevated level of the  $I_g$  will negatively influence the final LNA noise performance [28].

The minimum noise temperature  $T_{min}$  of the HEMT is well-known to appear at the bias for minimum  $\sqrt{I_d/g_{m,o}}$  [27], plotted in Fig. 2.1 (d). A smaller value of  $\sqrt{I_d/g_{m,o}}$  means that at a lower drain current, the transistor provides higher transconductance. Thus, a lower  $\sqrt{I_d/g_{m,o}}$  leads potentially to better noise performance at low-power bias, as discussed in [15]. The minimum  $\sqrt{I_d/g_{m,o}}$  value  $0.22 \sqrt{\text{V} \cdot \text{mm}/\text{S}}$  is observed at  $I_d = 16 \text{ mA/mm}$ . This  $\sqrt{I_d/g_{m,o}}$  performance is comparable to the state-of-the-art InP HEMT specifically optimized for low-power operation ( $0.21 \sqrt{\text{V} \cdot \text{mm}/\text{S}}$  at  $10 \text{ mA/mm}$ ) [16].

The lower the subthreshold swing (SS), the higher  $g_{m,o}/I_d$  the HEMT can achieve. Hence, the SS can determine the potential noise performance at low power consumption bias [29]. The SS of the InP HEMT characterized is plotted in Fig. 2.1 (e), from which  $18 \text{ mV/dec}$  SS can be observed nearly independent from  $V_{ds}$ . For comparison, state-of-the-art InP HEMT is  $14 \text{ mV/dec}$  at  $5 \text{ K}$  [15] and the lowest experimental values of FETs reported is  $11 \text{ mV/dec}$  at  $4.2 \text{ K}$  [30]. The data in Fig. 2.1 (d) and Fig. 2.1 (e) therefore suggest the

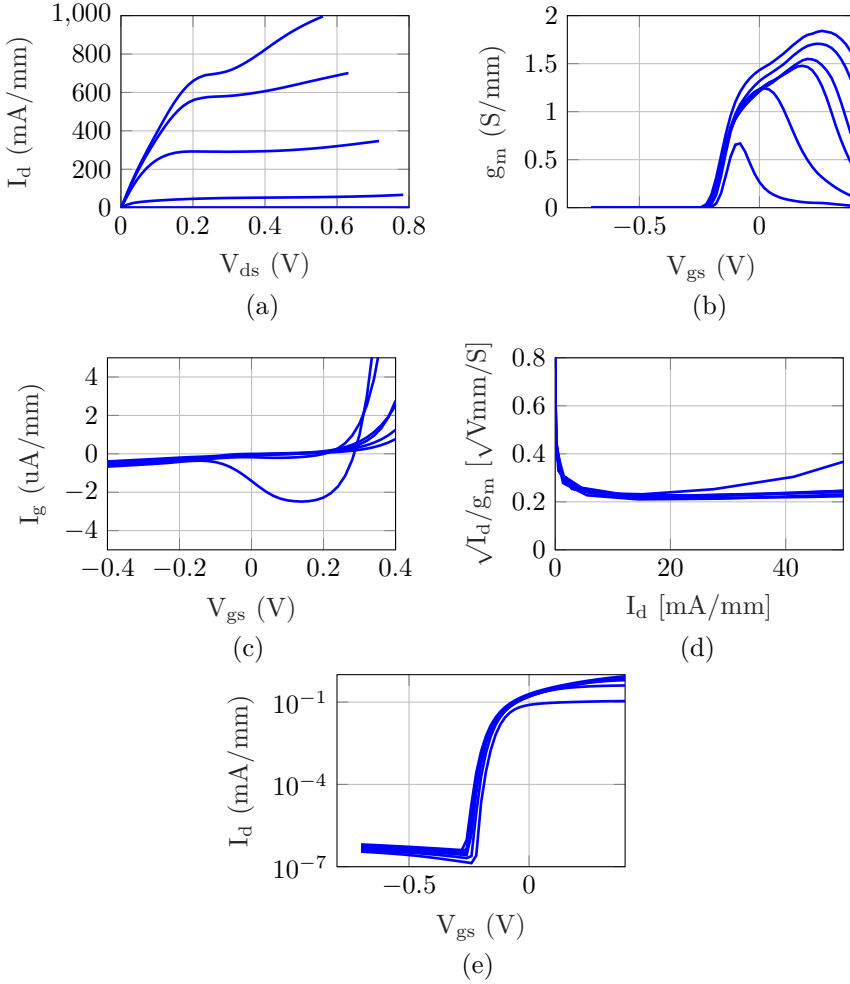


**Figure 2.1:** DC characterisation at 4 K of  $4 \times 50 \mu\text{m}$  InP HEMTs used in circuit design. (a)  $I_d$  versus  $V_{ds}$  where  $V_{gs}$  is from -0.5 V to 0.5 V in steps of 0.2 V.  $V_{ds}$  is from 0.05 to 0.8 V in steps of 0.15 V for (b)  $g_{m,o}$  versus  $V_{gs}$ ; (c)  $I_g$  versus  $V_{gs}$ ; (d) the  $\sqrt{I_d/g_m}$  versus  $I_d$ ; and (e) SS plot where  $I_d$  versus  $V_{gs}$  plot in log scale. [From Paper B]

potential of the InP HEMTs to be used for low-power cryogenic LNA circuit application.

## 2.2 Cryogenic small-signal noise model at low power

In superconducting quantum computing that demand low power consumption for large-scale systems, a comprehensive understanding of the HEMT model used in LNA design for qubit readout is crucial. This knowledge enables trade-offs in circuit design to meet the qubit readout requirements at low power. In this licentiate thesis, the small-signal noise model used to simulate the HEMT was based on Pospieszalski's noise model [28]. This model assigns the fitting parameters equivalent drain temperature  $T_d$  and gate temperature  $T_g$  to resistance and conductance, respectively, in a equivalent circuit model of the HEMT; See Fig 2.2. The small-signal noise model in this thesis adapted a mature small-signal equivalent circuit model for the HEMT, both at room temperature and cryogenic ambient studied in this work [31]. The parameters of this small-signal equivalent models were extracted from the S-parameters measured of the HEMT at targeted low-power biases at 4 K ambient temperature.

In Pospieszalski's noise model,  $T_g$  is set to be close to the ambient temperature. In contrast,  $T_d$ , which accounts for the hot electrons in the channel, is usually much higher than the ambient temperature.

Using Pospieszalski's noise model, the minimum noise temperature  $T_{min}$  that can be achieved by the HEMT under a certain bias is expressed by

$$T_{min} \approx 2 \frac{f}{f_T} \sqrt{R_t T_g g_{ds} T_d} \quad (2.1)$$

where  $R_t$  is the sum of the gate resistance  $R_g$ , the intrinsic gate-source resistance  $R_i$  and the source resistance  $R_s$ .  $g_{ds}$  denotes the intrinsic output conductance of the applied drain voltage. The intrinsic cut-off frequency  $f_T$  is described by [32]

$$f_T = \frac{g_m}{2\pi(C_{gs} + C_{gd}) \cdot (1 + \frac{R_s + R_d}{R_{ds}}) + g_m C_{gd}(R_s + R_d)} \quad (2.2)$$

where  $C_{gs}$  and  $C_{gd}$  are the intrinsic gate-source and gate-drain capacitance,

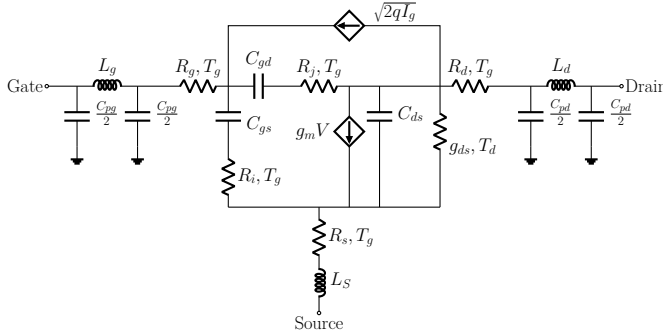


**Figure 2.2:** Equivalent small-signal and noise model of the InP HEMT. [From Paper B]

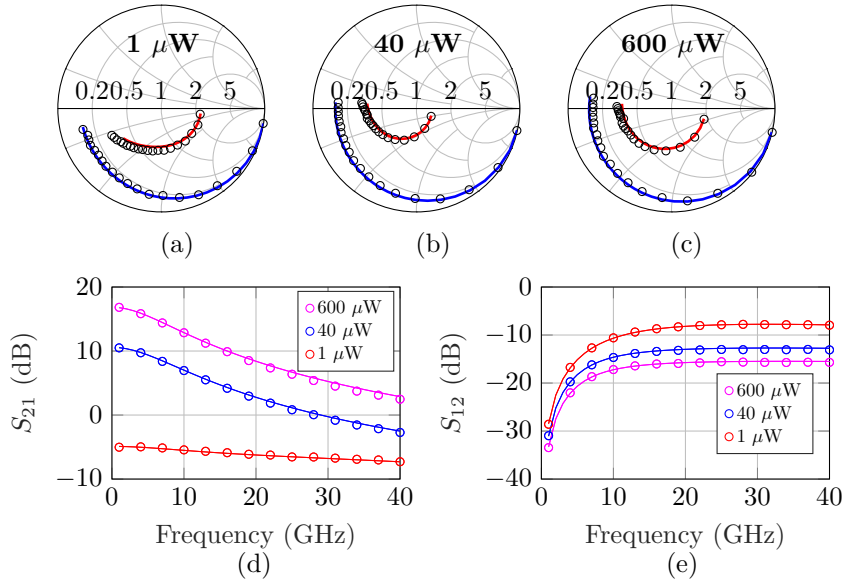
respectively,  $R_d$  is the drain resistance, and  $R_{ds}$  is the inverse of  $g_{ds}$ .  $g_m$  is the intrinsic transconductance.

The  $T_{min}$  are thus bias-dependent and have a close relationship with the extracted small-signal equivalent circuit parameters.

## HEMT small-signal model parameters at low power

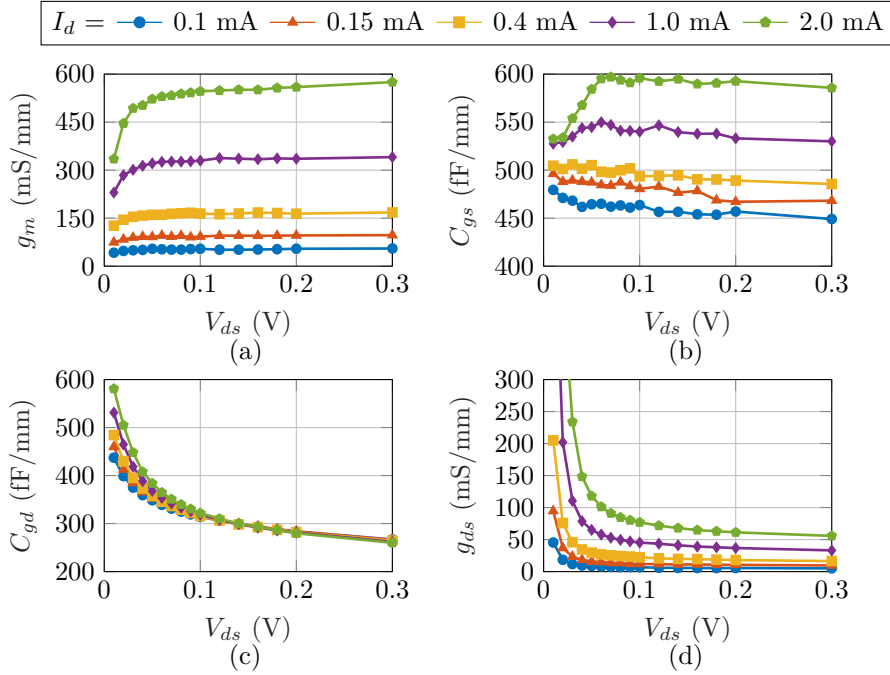
In this thesis, on-wafer measurements of the InP HEMT's S-parameters at 4 K were recorded using a Rohde Schwarz ZVA67 vector network analyzer with a maximum frequency range of 67 GHz. The InP HEMTs, same as described in Sec. 2.1, were tested at different  $V_{ds}$  and  $I_d$  levels, with dc power varying from 1  $\mu\text{W}$  to 600  $\mu\text{W}$ . Given that the magnitude of  $I_g$  was only a few tens of nA, the contribution of the gate current to the overall dc power consumption was considered negligible.

Fig. 2.3 depicts the comparison between the measured and simulated S-parameters of the InP HEMT at 4 K for dc power of 1, 40, and 600  $\mu\text{W}$ , up to 40 GHz. The simulated data was generated using the extracted small-signal parameters. A good agreement is observed between the measured and simulated S-parameters for all dc power levels. This confirms the accuracy and effectiveness of the extracted small-signal model over a wide range of bias powers.



**Figure 2.3:** Comparison of measured (circles) and simulated (solid) S-parameters from 0.01 to 40 GHz of a  $4 \times 50 \mu\text{m}$  gate width and 100 nm gate-length InP HEMT at 4 K for different ULP levels.  $S_{11}$  (red line) and  $S_{22}$  (blue line) plotted in Smith chart with bias power at (a)  $1 \mu\text{W}$  ( $V_{ds} = 0.01 \text{ V}$ ,  $I_d = 0.1 \text{ mA}$ ) (b)  $40 \mu\text{W}$  ( $V_{ds} = 0.04 \text{ V}$ ,  $I_d = 1 \text{ mA}$ ), and (c)  $600 \mu\text{W}$  ( $V_{ds} = 0.3 \text{ V}$ ,  $I_d = 2 \text{ mA}$ ). (d)  $S_{21}$  and (e)  $S_{12}$  for 600, 40, and  $1 \mu\text{W}$ . [From Paper B]

Fig 2.4 presents extracted  $g_m$ ,  $C_{gs}$ ,  $C_{gd}$ , and  $g_{ds}$  versus  $V_{ds}$  for different  $I_d$  at 6 GHz. As illustrated in Fig 2.4 (a), the dependence of  $g_m$  on  $I_d$  is strong, with a roll-off starting at  $V_{ds}$  of 0.05 V. The mean  $g_m$  values prior to roll-off are 50, 75, 160, 330, and 530 mS/mm for  $I_d$  of 0.1, 0.15, 0.4, 1, and 2 mA, respectively, indicating a nearly linear relationship with  $I_d$ . This roll-off intensifies for current biases exceeding 0.4 mA. When sweeping the  $V_{ds}$  from saturation to the triode region (0.3 V to 0.01 V) while keeping  $I_d$  fixed,  $g_m$  initially remains constant due to increased  $V_{gs}$  compensating for the reduced influence of  $V_{ds}$ . However, upon reaching low  $V_{ds}$  values, it is evident that the insufficient number of channel carriers for effective  $V_{gs}$  modulation results in a decrease in  $g_m$ .



**Figure 2.4:** Extracted (a) intrinsic  $g_m$ , (b)  $C_{gs}$ , (c)  $C_{gd}$ , (d)  $g_{ds}$  as a function of  $V_{ds}$  at 6 GHz of a  $4 \times 50 \mu\text{m}$  gate width and 100 nm gate-length InP HEMT at 4 K with  $I_d$  bias from 2 mA down to 0.1 mA. [From Paper B]

The  $C_{gs}$  behavior in Figs 2.4 (b) exhibits a similar pattern to the  $g_m$  for  $I_d$  values of 1 mA or higher. For  $I_d$  values of 0.4 mA or lower,  $C_{gs}$  undergoes a minor increase as  $V_{ds}$  decreases. This can be explained by the interplay between the overlapping effect of  $V_{ds}$  and  $V_{gs}$  on  $C_{gs}$  at a constant  $I_d$ . When  $V_{ds}$  was lowered, an increased  $V_{gs}$  needed to sustain the fixed  $I_d$  enhanced the channel's carrier concentration and slightly raised  $C_{gs}$ . On the other hand, a reduction in  $V_{ds}$  resulted in a more uniform 2DEG carrier distribution, decreasing the carrier density at the source side and subsequently lowering  $C_{gs}$ . At high current bias (and high  $V_{gs}$ ), the channel carrier concentration reaches saturation, causing the influence of low  $V_{ds}$  to become dominant, leading to

a decrease in  $C_{gs}$ . Conversely, at low drain current where  $V_{gs}$  is low and the channel is not fully open, it is expected that the increase in  $V_{gs}$  at lower  $V_{ds}$  will outweigh the decrease in  $V_{ds}$ , resulting in an increase in  $C_{gs}$ .

$C_{gd}$  in Figs 2.4 (c) displays no substantial  $I_d$  dependency for  $V_{ds}$  greater than 0.1 V. However, when  $V_{ds}$  is below this bias,  $C_{gd}$  escalates 2 to 6 times more swiftly, depending on  $I_d$ . The  $C_{gd}$  increase can be attributed to the reduction of the depletion region of the 2DEG at the drain side.

The extracted  $g_{ds}$  values exhibit an increase with higher  $I_d$ , as plotted in Figure 2.4 (d). When  $V_{ds}$  enters triode region (0.03 to 0.07 V), the HEMT channel behaves as a voltage-controlled resistor and small fluctuations in  $V_{ds}$  result in significant current variations. This phenomenon explains the observed increase in  $g_{ds}$ .

The extracted small-signal model parameters reveal evident trends when the InP HEMT is biased at low power. All parameters exhibit relatively weak responses to a decrease in  $V_{ds}$  until reaching a value of around 0.05 V for the measured InP HEMT. This observation suggests that the InP HEMT can preserve its microwave performance even at exceptionally low power in cryogenic conditions, a characteristic desired for large-scale qubit readout. Slightly below  $V_{ds} = 0.05$  V,  $g_m$  drops sharply, accompanied by a rise in  $g_{ds}$  and the overall intrinsic capacitance. Based on Eqs. (2.1) and (2.2), a rapid deterioration in  $f_T$  and  $T_{min}$  is anticipated.

## HEMT noise model and extraction at low power

In Pospieszalski's model, all noise parameters and associated gain of the transistor are based on small-signal equivalent circuit model parameters,  $T_g$ , and  $T_d$ . Gate leakage noise is modeled as a shot noise source, as depicted in Fig.2.2, with noise current  $\sqrt{2 \cdot q \cdot I_g}$ . The  $I_g$  values are measured during the S-parameter measurements at each bias point. For the targeted second stage amplification of qubit readout at 4 K,  $T_g$  is set to 10 K to account for potential self-heating in the device [27], [33]–[35]. With the extracted small-signal equivalent circuit model parameters of the InP HEMT under different biases,  $T_d$  can be extracted by fitting the simulated noise of the HEMT model to the measured noise results.

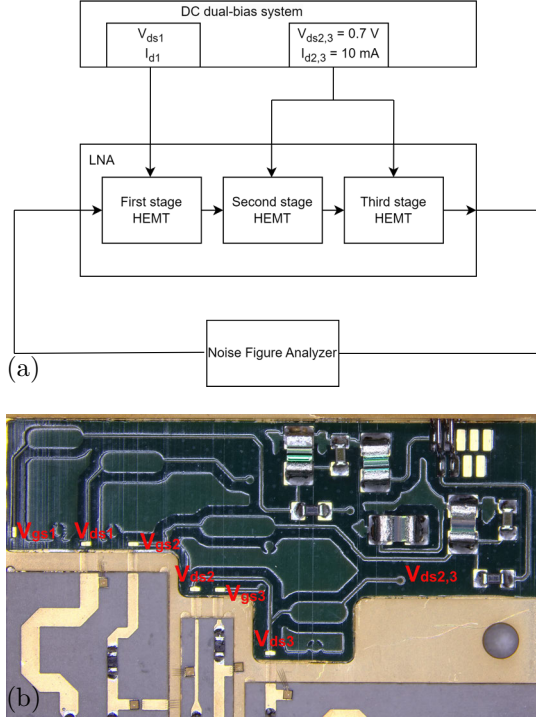


**Figure 2.5:** (a) Schematic of the dual-bias noise extraction method [From Paper B].  $I_{d1}$  and  $I_{d2,3}$  are adjusted by gate voltage of each stage:  $V_{gs1}$ ,  $V_{gs2}$ , and  $V_{gs3}$ , which are denoted in (b) top view of the fabricated dc bias printed circuit board (PCB) circuit.

### Dual-bias strategy for low power noise model extraction

Due to insufficient gain and low noise signal levels, on-wafer noise measurements for HEMTs at cryogenic temperatures suffer from low accuracy. Thus, an indirect noise parameters extraction method using a hybrid amplifier equipped with the HEMTs was adapted [14], [36]. The InP HEMTs were mounted in a three-stage 4-8 GHz LNA with the same gate and drain bias for all stages for noise measurement and  $T_d$  fitting. Such a procedure results in much higher signal-to-noise ratio as required by the noise figure analyzer (NFA). In this work where the low-power regime was of particular interest, the hybrid LNA

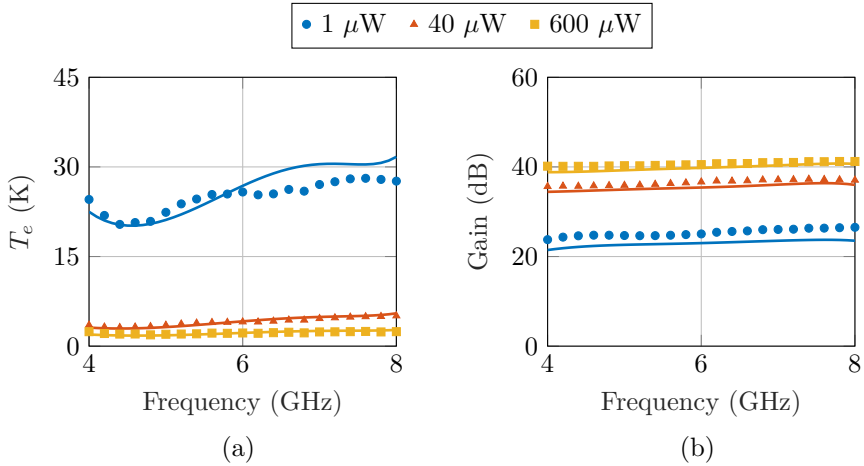


**Figure 2.6:** Comparison of measured (symbols) and modeled (solid lines) (a) noise and (b) gain of the 4-8 GHz LNA used for  $T_d$  extraction at 4 K for the first stage HEMT biased at  $1 \mu\text{W}$  ( $V_{ds1} = 0.01 \text{ V}$ ,  $I_{d1} = 0.1 \text{ mA}$ ),  $40 \mu\text{W}$  ( $V_{ds1} = 0.04 \text{ V}$ ,  $I_{d1} = 1 \text{ mA}$ ), and  $600 \mu\text{W}$  ( $V_{ds1} = 0.3 \text{ V}$ ,  $I_{d1} = 2 \text{ mA}$ ). The second and third HEMT stages were biased with  $V_{ds2,3} = 0.7 \text{ V}$ ,  $I_{d2,3} = 10 \text{ mA}$ ; See Fig. 2.5.

method still suffered from insufficient gain for accurate  $T_d$  extraction. This was solved by replacing the common bias for the HEMTs in the LNA with a dual-bias design. In this way, gain for the LNA could be preserved also at very low dc power in the HEMT down to  $1 \mu\text{W}$ . The dual-bias circuit was implemented in the LNA to supply  $V_{gs}$  and  $V_{ds}$  independently for the first stage, as well as the second and third stages, respectively. See Fig 2.5. The first-stage InP HEMT was biased as in the S-parameter measurement. In contrast, the second and third InP HEMTs were biased at previously extracted and modeled bias point for high gain and low noise ( $V_{ds} = 0.475 \text{ V}$  and  $I_d = 5 \text{ mA}$ ). Fig 2.6 shows the noise and gain measurements and simulations of the LNA over the frequency range of 4 to 8 GHz at three bias powers ( $1 \mu\text{W}$ ,  $40 \mu\text{W}$ , and  $600 \mu\text{W}$ ) for the first stage InP HEMT. The LNA with the dual-bias solution can sustain more than 20 dB gain when the first stage InP HEMT is biased at  $1 \mu\text{W}$ . The measured equivalent noise  $T_e$  at  $1 \mu\text{W}$  is around 20 K. The agreement between simulated and measured data for both gain and noise

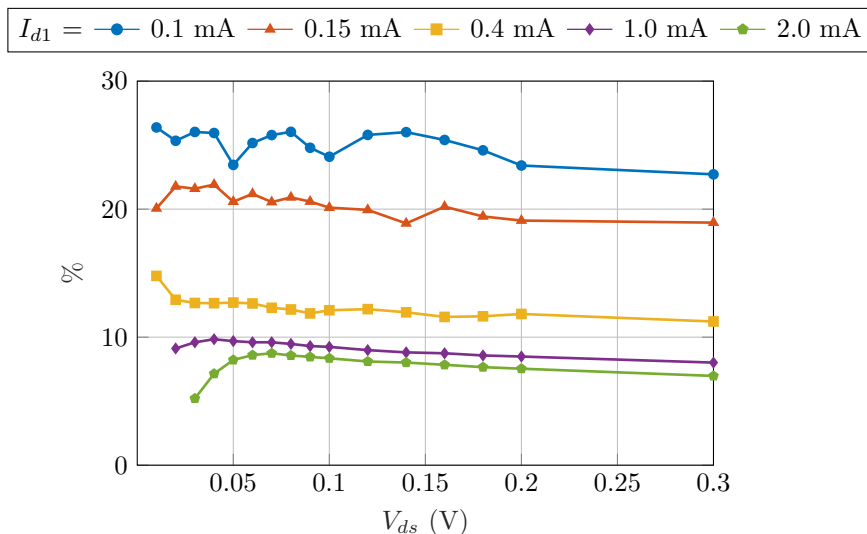


**Figure 2.7:** Simulated percentage of second and third-stage noise contribution to the total LNA noise versus first stage InP HEMT  $V_{ds}$  for different  $I_{d1}$ .

is excellent for 40 and 600  $\mu\text{W}$  bias. The agreement is slightly worse for 1  $\mu\text{W}$  bias, which can be attributed to measurement uncertainty due to lower gain and non-uniformity between HEMTs especially at low power.

For a meaningful low-power  $T_d$  extraction, the measured total noise should be highly correlated with the noise contribution from the first stage transistor. By setting  $T_d$ ,  $T_g$  and ambient temperature  $T_a$  of the first stage HEMT and input matching network to zero in the simulator (AWR Microwave Office), the contribution of the subsequent stages can be obtained. The simulated equivalent noise  $T_e$  percentage of the second and third stages to the overall  $T_e$  of the LNA at 6 GHz are plotted versus  $V_{ds}$  of the first stage InP HEMT for different  $I_{d1}$  in Fig 2.7. Despite the increasing noise contribution for lower first stage  $I_{d1}$ , the first stage InP HEMT still contributes more than 70% noise temperature even at  $I_{d1} = 0.1$  mA. As a result, the indirect procedure for measuring noise of the first InP HEMT in a three-stage LNA can be used with sufficient gain and hence noise accuracy even when biasing this first stage at a dc power of only 1  $\mu\text{W}$  (first stage InP HEMT  $V_{ds} = 0.01$  V).

### HEMT noise model parameters at low power

The extracted  $T_d$ , noise parameters, and associated gain of the InP HEMT at 6 GHz are presented versus  $V_{ds}$  for different  $I_d$  under a 4 K ambient temperature in Fig. 2.8.

In Fig. 2.8 (a), the extracted  $T_d$  values are shown. A decrease in  $I_d$  results in a proportional reduction in  $T_d$ , confirming the widely accepted observation [37] that  $T_d$  exhibits a nearly linear relationship with  $I_d$ . From a device physics perspective,  $T_d$  represents the amount of fluctuations among channel electrons [38]. It is expected that electron scattering diminishes with reduced dc power in the channel, which explains the decline in  $T_d$  with lower  $V_{ds}$  bias.

Using Eq. (2.1),  $T_{min}$  was calculated from the extracted  $T_d$  and small-signal model parameters. In Fig. 2.8 (b),  $T_{min}$  of the InP HEMT is depicted. As  $I_d$  increases,  $T_{min}$  improves and saturates beyond 1 mA. When  $V_{ds}$  is above 0.05 V,  $T_{min}$  stays constant or even slightly decreases with a lower  $V_{ds}$ . According to Eqs. (2.1) and (2.2), the increase in  $T_{min}$  below the critical  $V_{ds}$  around 0.05 V is primarily due to the deterioration of the small-signal model parameters, as  $T_d$  is a monotonically decreasing function for  $I_d$  below 2.0 mA. Consequently, the small-signal behavior in Fig. 2.4 serves as a useful indicator for  $T_{min}$  performance, in particular under low-power conditions. The observed slightly decrease in  $T_{min}$  with lower  $V_{ds}$  before 0.05 V is mainly due to the fact that the positive impact of the reduced  $T_d$  outweighs the negative impact of the degradation in small-signal model parameters.

From Fig. 2.8 (b), the optimal bias point for achieving the lowest  $T_{min}$  with minimal dc bias power can be determined for the InP HEMT at 4 K. In a single-stage analysis of HEMT LNA design, the overall noise performance must take other noise parameters into account in relation to impedance matching:

$$T_e = T_{min} + T_0 \frac{R_n}{\Re Z_{opt}} |Z_s - Z_{opt}|^2 \quad (2.3)$$

where  $T_0$  is the reference temperature (290 K),  $R_n$  is the noise resistance,  $Z_s$  is the source impedance, and  $Z_{opt}$  is the optimal impedance for noise matching. To achieve the minimum  $T_e$  across the entire bandwidth of the cryogenic LNA, the impact of  $R_n$  and  $Z_{opt}$  is crucial.

In a multi-stage HEMT LNA, the associated gain  $G_{assoc}$  for each stage must be considered [39]. The parameter  $N$  is introduced as an invariant to account for the combined effect of  $R_n$  and  $\Re(Z_{opt})$ , as defined in [40]:

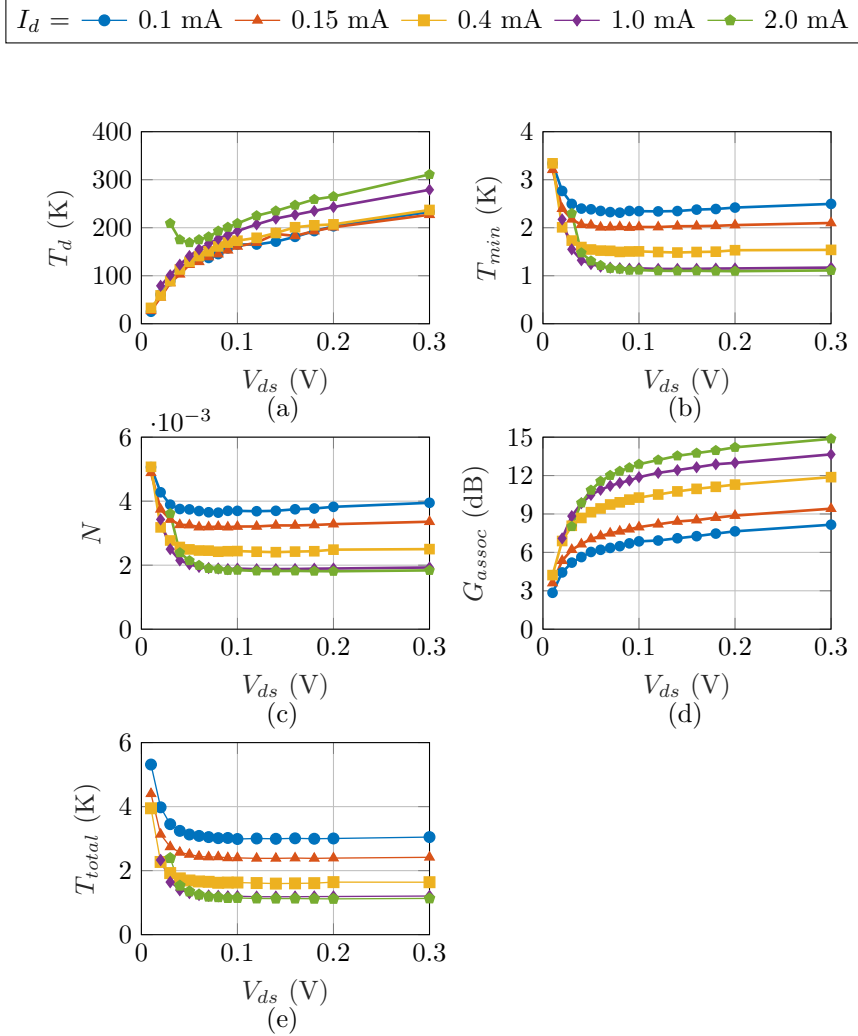


**Figure 2.8:** Extracted (a)  $T_d$ , (b)  $T_{min}$ , (c)  $N$ , (d)  $G_{assoc}$ , and (e)  $T_{total}$  as a function of  $V_{ds}$  at 6 GHz for a  $4 \times 50 \mu\text{m}$  gate width and 100 nm gate-length InP HEMTs at 4 K with  $I_d$  biased from 2 mA down to 0.1 mA.

$$N = \frac{R_n}{\Re(Z_{opt})} \quad (2.4)$$

At frequencies much lower than  $f_T$ ,  $N$  is proportional to  $T_{min}$  [28]. This is confirmed in Fig. 2.8 (c) where  $N$  displays the same trend as  $T_{min}$  in Fig. 2.8 (b). Below  $V_{ds} = 0.05$  V,  $N$  rapidly increases for all  $I_d$  values, causing the InP HEMT to become more sensitive to noise mismatch.

As depicted in Fig. 2.8 (d), the  $G_{assoc}$  declines for lower  $I_d$  values. Similar to other noise parameters,  $G_{assoc}$  decreases gradually with reduced  $V_{ds}$  and drops off sharply when reaching the critical point at  $V_{ds} = 0.05$  V. It is noteworthy that at a dc power of only  $40 \mu\text{W}$  ( $V_{ds} = 0.04$  V;  $I_d = 1$  mA), the InP HEMT still maintains a  $G_{assoc}$  of 10 dB at 6 GHz.

To study the influence of  $G_{assoc}$  in the cascade noise analysis, a modified noise measure  $M_{opt}$  is introduced. Compared to the original definition of noise measure [41], available gain and  $T_n$  is replaced by  $G_{assoc}$  and  $T_{min}$ :

$$M_{opt} = \frac{T_{min}}{T_0} \frac{1}{1 - \frac{1}{G_{assoc}}} \quad (2.5)$$

The total noise temperature ( $T_{total}$ ) of an infinite number of cascade stages is

$$T_{total} = T_0 \cdot M_{opt} \quad (2.6)$$

The  $T_{total}$  is plotted in Fig. 2.8 (e), which exhibits a pattern similar to that of  $T_{min}$ . However, the critical  $V_{ds}$ , where performance degrades, slightly increases from 0.05 to 0.07 V. This is due to the rapid decrease of  $G_{assoc}$  with  $V_{ds}$  compared to  $T_{min}$ . The  $T_{total}$  constitutes a more stringent condition compared to  $T_{min}$  for choosing the first stage HEMT minimum bias. The projected  $Z_{opt}$  in the Smith chart in Fig. 2.9 shows that the lower the bias power, the further away  $Z_{opt}$  is from the origin of the Smith chart, emphasizing the challenge in impedance matching between noise and bandwidth at low power.

In summary, a cryogenic small-signal noise model for the InP HEMT reaching a dc power of  $1 \mu\text{W}$  was presented. It was found that noise parameters and  $G_{assoc}$  were strongly influenced by  $I_d$ . The impact of  $V_{ds}$  on noise parameters is relatively insignificant above  $V_{ds} = 0.05$  V. Below this, noise performance and  $G_{assoc}$  rapidly deteriorate. Thus, maintaining  $V_{ds}$  above this level can help prevent noise degradation, serving as a key guideline for optimizing low power in cryogenic HEMT LNA design. The behavior observed in the InP

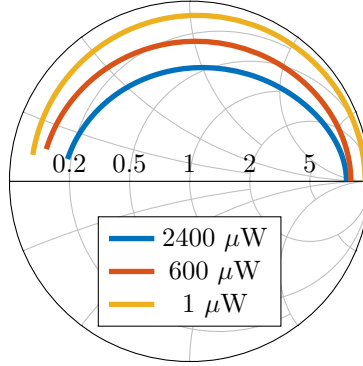


**Figure 2.9:** The extracted  $Z_{opt}$  at 4 K of a  $4 \times 50 \mu\text{m}$  gate width and 100 nm gate-length InP HEMT with bias power of 2.4 mW ( $V_{ds} = 0.475 \text{ V}$ ,  $I_d = 5 \text{ mA}$ ), 600  $\mu\text{W}$  ( $V_{ds} = 0.3 \text{ V}$ ,  $I_d = 2 \text{ mA}$ ), and 1  $\mu\text{W}$  ( $V_{ds} = 0.01 \text{ V}$ ,  $I_d = 0.1 \text{ mA}$ ) at 4 K in the Smith chart. The data is plotted up to 40 GHz

HEMT small-signal noise model under cryogenic conditions at low power indicates the feasibility of attaining low noise levels while also maintaining a reduced dc bias power. However, potential challenges related to wide-band matching and gain could arise. The next chapter will address these issues by detailing the analysis and implementation of a low-power LNA specifically tailored for qubit readout applications, based on the investigated small-signal noise model presented in this chapter.



## CHAPTER 3

---

### Low-power HEMT LNA design for qubit readout

---

Utilizing the extracted cryogenic ULP small-signal noise model of the InP HEMT in Chapter 2, low-power optimization of the HEMT LNA for qubit readout becomes possible. This implies a trade-off between noise and low-power performance for the HEMT LNA. The analysis in Chapter 2 tells us that low-power design also means a decrease in  $G_{assoc}$  and poor matching conditions for the HEMT. Finally, the low-power optimization must meet the system requirements in qubit amplification with respect to gain, bandwidth, and linearity.

In this chapter, the design objectives of the low-power HEMT LNA for qubit readout will be analyzed, taking into account the quantum system constraints. The HEMT small-signal noise model developed in Chapter 2 will be applied in the design of a tailored hybrid LNA to achieve the optimal balance between noise performance and power consumption. A suspended transmission line structure in the designed LNA is implemented in a cryogenic vacuum environment to meet the high impedance requirement for noise matching. The measured results of the LNA will be compared with electromagnetic (EM) and circuit schematic co-simulation results. The realized LNA at low power shows state-of-the-art noise performance making it interesting for qubit readout in

future quantum computing.

### **3.1 Design analysis for qubit readout**

In Chapter 1, the HEMT LNA in a qubit experimental setup was described. The HEMT LNA is located as the second amplifier after the parametric amplifier at the 4 K stage which provides 1 to 1.5 W cooling capacity. Several isolators are put in between the parametric amplifier and HEMT LNA to prevent noise from the HEMT LNA's input from reaching the fragile qubits [2], [4], [10]. In some experiments, the HEMT LNA is employed as first stage amplifier at 4 K, i.e without parametric amplifier, to amplify the qubit resonator with sufficient readout fidelity [6].

In qubit readout systems, present (commercial) HEMT LNAs are normally optimized for minimum noise, with a typical  $T_e$  ranging between 1.5 and 2 K and a gain of around 40 dB [3]. The HEMT LNA has a bandwidth of 4-8 GHz and consumes dc power on the order of 5-10 mW [1], [26].

Amplifier linearity is an essential design parameter since each LNA handles simultaneous qubit readout. The line-width and frequency separation between each readout signal can be designed to be below 11 MHz and 160 MHz, respectively [42]. In an ideal scenario, the available frequency band should be fully utilized for qubit readout signal separated with the smallest possible frequency distancing. Assuming each qubit occupies a 2 MHz bandwidth, the ideal capacity for a 4-8 GHz cryogenic LNA is 2000 qubits. Utilizing the full 4 GHz bandwidth for qubit readout increases the input linearity requirement by +33 dB compared to an LNA used for single qubit readout. If the preceding stage parametric amplifier achieves an output 1 dB compression point P1dB of around -90 dBm [43], the input P1dB for the HEMT LNA should be at least higher than -57 dBm. In reality, the qubit handling capability across a given bandwidth in the HEMT LNA is considerably smaller, due to many practical limitations.

In superconducting quantum computing, the readout process is designed not to directly interact with the qubit, but instead to probe using a superconducting resonator. This is called dispersive readout. This allows the readout system to acquire information about the state of the qubit while effectively minimizing unwanted "back-action" effects on the qubit [5]. Top part of Fig. 3.1 shows the equivalent circuit representation of a dispersive read-

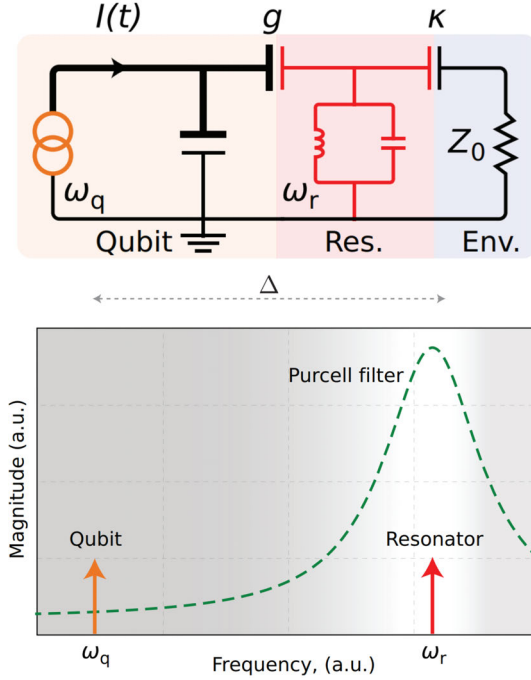


**Figure 3.1:** Top: circuit representation of qubit ( $\omega_q$ ) coupling to environment load with a readout resonator ( $\omega_r$ ) in-between. Bottom: Transmission spectrum of the resonator frequency and qubit frequency. The Purcell filter (green dashed line), enhancing fast readout and mitigating qubit decay, is not denoted in the top figure. [5]

out. A resonator is situated between the qubit and the readout environment load ( $50 \Omega$ ). The resonator placement serves two functions: firstly, it shields the qubit from potential decay, and secondly, it introduces a detuning that shifts the readout frequency away from the native qubit frequency  $\omega_q$ . As illustrated in Fig. 3.1 bottom part, the qubit resonator readout frequency,  $\omega_r$ , is distanced from  $\omega_q$  by a frequency detuning  $\Delta$ :

$$\omega_r = \omega_q \pm \Delta \quad (3.1)$$

Here,  $\omega_r/2\pi$  and  $\Delta/2\pi$  range from typically 4-8 GHz [1] and 0.5-1.5 GHz [10], respectively.  $\omega_r$  can be engineered over a wide frequency range in qubit

resonator fabrication. This suggests that the 4-8 GHz working bandwidth requirement for the HEMT LNA can be traded off versus other design parameters such as dc power. State-of-the-art TWPA [44] uses 3.5-5.5 GHz and JPA [45] uses 4.6-4.8 GHz for qubit readout. Provided that the low-power LNA allows for an increase in the feasible number of qubit readouts within the limited cooling power capability, the bandwidth of the LNA can therefore be reduced for lower dc power consumption. The small-signal noise model in Chapter 2 shows that such a trade-off must be carefully balanced with gain and matching when running the HEMT at low power.

To design a low-power cryogenic LNA optimized for superconducting qubit readout, the following priorities must be taken into consideration:

1. Reducing the LNA's power consumption below 1 mW [1].
2. Maintaining adequate noise performance ( $\leq 2$  K) for qubit readout.
3. Ensuring sufficient linearity ( $\geq -60$  dBm) of the LNA to support the maximum number of qubit readouts.

## **3.2 Design and implementation of low-power LNA for qubit readout**

In this thesis, a design goal of the low-power LNA for qubit readout was to consume less than 200  $\mu$ W dc power, which is much less than the current 5-10 mW used today [1]. The noise temperature of the low-power LNA was targeted to 2 K which meet the requirement for qubit readout at 4 K ambient temperature [3]. As a trade-off for the low-bias power, the targeted gain and working bandwidth were set to be above 20 dB and 4-6 GHz. This is due to the high sensitivity of the matching difficulty and associated gain of the HEMT to bias power revealed by the extracted model versus power in Chapter 2.

In this thesis, the developed HEMT LNA utilized hybrid technology for optimal noise performance. This approach allows for low-loss matching and easy prototyping, advantages that MMIC technology currently does not offer. A common-source topology was applied for low noise, high gain, high isolation, including the capability to use inductive source degeneration. From experience, a transistor size with a  $4 \times 50$   $\mu$ m gate-width was chosen for the

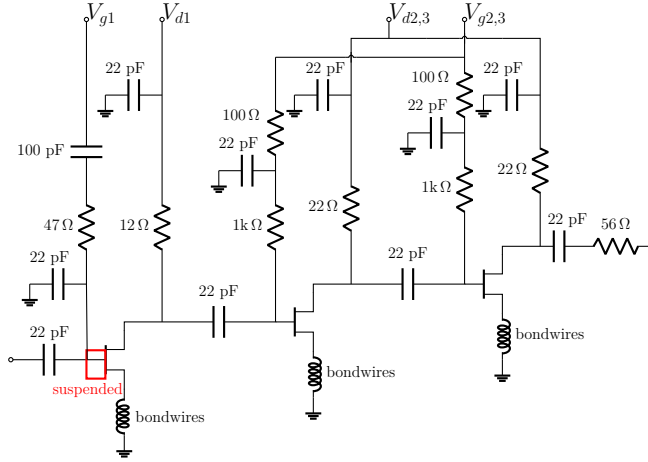


**Figure 3.2:** Circuit schematic of the designed 4-6 GHz cryogenic HEMT LNA. The red frame represents the suspended transmission line. [From Paper B]

InP HEMT technology, as its gate impedance is more readily matched at C band frequencies.

The simplified circuit schematic of the LNA can be seen in Fig. 3.2. Based on the cascade noise equation by Friis [39], the first-stage HEMT is anticipated to contribute the most noise, provided the first stage HEMT has adequate gain. Considering the rapid degradation of the InP HEMT’s  $G_{assoc}$  (Fig.2.8 (d)) and  $Z_{opt}$  (Fig.2.9) at a reduced dc bias, it is reasonable to bias the first-stage HEMT at higher power compared to the second and third-stage HEMT. The dual-bias dc system described in Fig. 2.5 was integrated into the LNA module. To sustain a  $G_{assoc}$  higher than 10 dB, the first HEMT stage was biased with  $V_{d1} = 0.08$  V and  $I_{d1} = 1.5$  mA, corresponding to  $90 \mu\text{W}$  ( $V_{ds} = 0.06$  V and  $I_d = 1.5$  mA) on the InP HEMT, with a  $12 \Omega$  stability resistor in series with the bias line. The second and third stages were biased with  $V_{d2,3} = 0.08$  V and  $I_{d2,3} = 1$  mA, respectively, with a  $22 \Omega$  stability resistor. The corresponding dc power for each InP HEMT of second and third-stages was  $30 \mu\text{W}$  ( $V_{ds}$  and  $I_d$  were 0.06 V and 0.5 mA) respectively.

To reduce the noise contribution of the second and third-stage HEMTs, it was critical to match the first-stage HEMT for the lowest noise with a sufficient gain. To achieve the simultaneous matching of noise and gain for the first-stage HEMT, the inductive source degeneration technique that can alter input

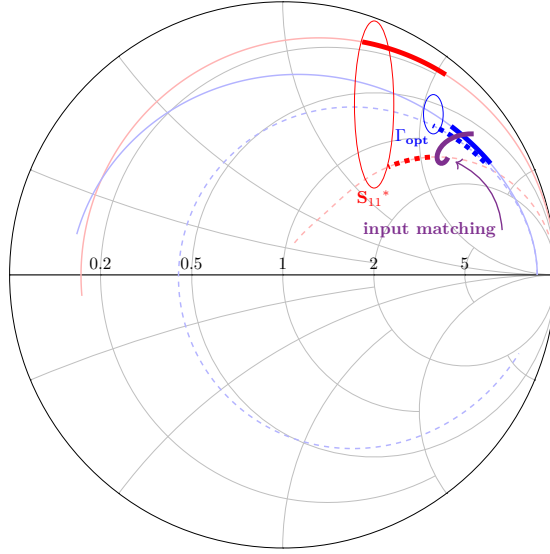


**Figure 3.3:** Simulated  $\Gamma_{opt}$  and conjugate  $S_{11}$  at 4 K of a  $4 \times 50$  nm gate-length and 100 nm gate-width InP HEMT biased at  $V_{ds} = 0.06$  V and  $I_d = 1.5$  mA up to 40 GHz. The dashed lines represent  $\Gamma_{opt}$  and  $S_{11}$  for the HEMT with two 1.6 mm long bond wires connected at the source using the inductance degeneration technique. The  $S_{22}$  of the input matching circuit was plotted at the purple solid line. The targeted frequency band from 4 to 6 GHz is marked in bold line.

impedance was applied. The introduced inductance is expected not to heavily influence the  $\Gamma_{opt}$ . However, the inductance will negatively affect available gain. The trade-off has been optimized to achieve lowest noise and highest gain in the simulation. The inductive source degeneration for the first-stage HEMT matching was implemented by two 1.6 mm bond wires connecting the source pad to the ground plane. Fig.3.3 demonstrates the simulated input matching using the inductive source degeneration in the Smith chart. The introduced source inductance adjusted the conjugate  $S_{11}$  much closer to the middle of the Smith chart. Meanwhile, the source degeneration only slightly influenced  $\Gamma_{opt}$  within the targeted 4-6 GHz frequency band. As a result, this approach brought the input impedance and  $\Gamma_{opt}$  closer together, making it easier to achieve simultaneous matching.

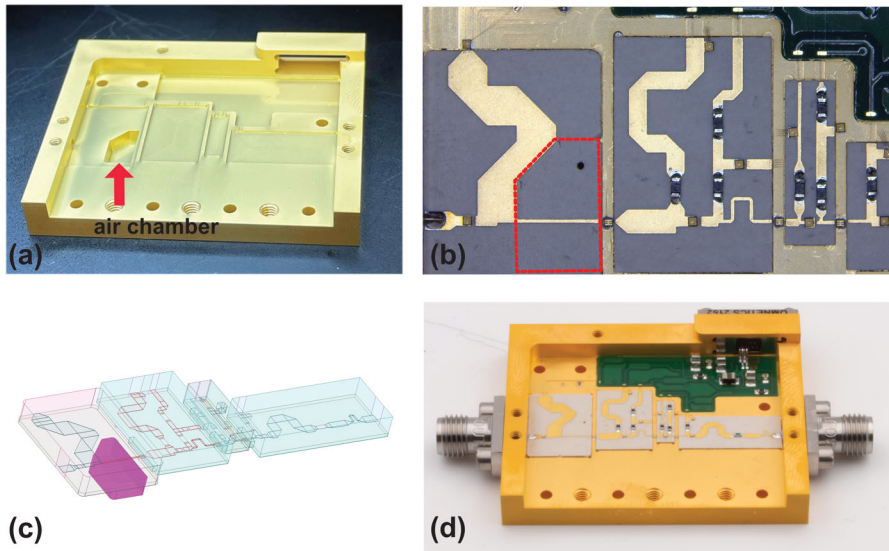


**Figure 3.4:** (a) The open chassis showing the air chamber for the suspended transmission line in the input matching network [From Paper A]. (b) Top view of the RF PCBs, the dashed line areas shows the suspended transmission line of the input matching network and venting aperture. (c) Ansys HFSS EM simulation model of the designed 4-6 GHz LNA. (d) The gold-plated open module with mounted RF and DC PCBs. The size of the full module is  $34.9 \text{ mm} \times 42.5 \text{ mm} \times 3 \text{ mm}$  [From Paper A].

A suspended transmission line was implemented to provide the high impedance needed for the input matching network, shown as the purple solid line in Fig. 3.3. The suspended transmission line provided  $277 \Omega$  impedance at 5.5 GHz. It was realized using a 2 mm deep air chamber beneath the substrate in the circuit package, shown as Fig 3.4 (a). Since the LNA is usually tested and used in the vacuum condition for cryogenic temperature, a venting aperture was designed to provide an airway that prevented the negative pressure to tear up the PCB above the air chamber, illustrated in Fig 3.4 (b). The structure of suspended line, venting aperture, and chassis chamber has been optimized with the EM simulation in Ansys HFSS, as shown in Fig 3.4 (c).

The second and third-stage HEMT both used four 0.2 mm source bond wires as inductive source degeneration to mitigate the matching difficulty.

The second stage HEMT is matched for higher gain compared to the first stage, and the third stage HEMT is matched solely for maximum gain. At the output matching stage, a  $56 \Omega$  series resistor was used to enhance the LNA stability. The designed LNA exhibited unconditional stability in the circuit simulation [46].

All matching PCBs used in the LNA were constructed using a 0.381 mm thick Duroid 6002 substrate with 0.0012 loss tangent and 2.94 relative permittivity. The RF circuit PCBs and dc bias PCB were fabricated and packaged in a gold-plated aluminum chassis with SMA coaxial RF connectors and connected with bond wires. Fig. 3.4 (d) shows the open chassis of the fabricated three-stage hybrid HEMT LNA.

### 3.3 Measurement results and discussion

The fabricated HEMT LNA circuit was characterized at 4 K for noise temperature, small-signal gain, return loss, and P1dB.

Using a Y-factor method with an in-house 20 dB cold attenuator at 4 K [47] and a 4-8 GHz LNA connected at the output to maintain a high signal-to-noise ratio for optimal measurement accuracy, the noise temperature and gain of the fabricated LNA module were measured by an Agilent N8975B noise figure analyzer. A noise measurement uncertainty of  $\pm 0.3$  K and measurement repeatability of  $\pm 0.1$  K were estimated [41].

At a total dc power of 200  $\mu$ W with  $V_{d1} = 0.08$  V and  $I_{d1} = 1.5$  mA, and  $V_{d2,3} = 0.08$  V and  $I_{d2,3} = 1$  mA, the simulated and measured gain and noise of the fabricated cryogenic LNA at 4 K are presented in Fig. 3.5. The good agreement between the measured results and simulations validates the extracted small-signal and noise model parameters at low power. The average gain across the target frequency band is 23.1 dB. Additionally, the measured LNA's average noise temperature  $T_{e,avg}$  is 2.0 K, with a minimum value of 1.7 K at 5.7 GHz. The measured 2.0 K noise temperature of the LNA reached the threshold necessary for qubit readout [3]. In some scenarios of qubit readout, LNA gain exceeding 20 dB is needed to compensate for losses from 4 K to 300 K. A higher gain can be achieved either by incorporating an additional stage in the HEMT LNA or by adding a LNA at the 77 K stage in the qubit readout chain.

Fig. 3.6 shows the dc power sweep of the fabricated cryogenic LNA, ranging

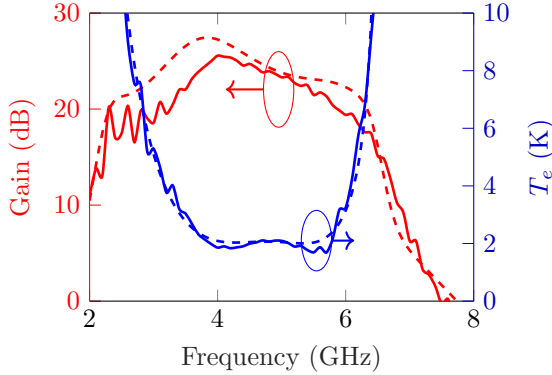


**Figure 3.5:** Simulated and measured gain and noise under cryogenic environment (4 K) for the designed 200  $\mu\text{W}$  InP HEMT LNA ( $V_{d1} = 0.08$  V and  $I_{d1} = 1.5$  mA, and  $V_{d2,3} = 0.08$  V and  $I_{d2,3} = 1$  mA). The red solid line is measured gain performance and the red dashed line is simulated gain performance. The blue solid line is the measured noise temperature and the blue dashed line is the simulated noise temperature. [From Paper B]

from 48  $\mu\text{W}$  to 600  $\mu\text{W}$ . The behavior of the  $T_{e,avg}$  with reduced bias power is similar to that of  $T_{min}$  shown in Fig. 2.8 (d). The decrease in gain at lower power is due to the degraded  $G_{assoc}$  in the lower  $V_{ds}$  range, as illustrated in Fig. 2.8 (d). When reduced to 100  $\mu\text{W}$  dc power, the LNA reaches an average gain of 22.5 dB and a  $T_{e,avg}$  of 2.6 K, with a minimum value of 2.0 K at 5.7 GHz. The best noise performance occurs at 600  $\mu\text{W}$ , with a  $T_{e,avg}$  of 1.6 K and a minimum value of 1.4 K at 5.7 GHz, and an average gain of 33.6 dB. A higher bias power at the first stage brings the  $T_{e,avg}$  closer to  $T_{min}$  for the designed bandwidth, indicating a relaxation of the trade-off between noise performance and bandwidth, which is predicted by the extracted small-signal noise model in Chapter 2.

Using a Keysight N52478 PNA-X network analyzer, the S-parameters and P1dB were measured at 4 K. The measured average  $S_{11}$  of the designed LNA biased at 200  $\mu\text{W}$  from 4-6 GHz is -8.9 dB, with the lowest value being -13.5 dB. Given the 60 dB isolation from isolators between the parametric amplifier and the HEMT LNA [4],  $S_{11}$  becomes less crucial in the qubit readout system. The average  $S_{22}$  is -18.7 dB.

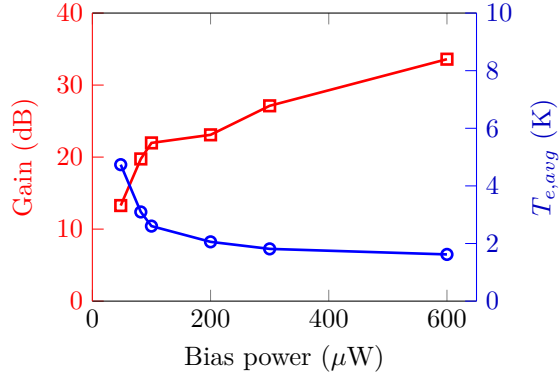


**Figure 3.6:** Measured average gain (red square line) and noise temperature (blue circle line) as a function of the total dc power from 48 to 600  $\mu\text{W}$  for the 4-6 GHz LNA at 4 K. Bias points are 48  $\mu\text{W}$  ( $V_{ds1} = 0.04$  V,  $I_{d1} = 0.6$  mA, and  $V_{ds2,3} = 0.04$  V,  $I_{d2,3} = 0.6$  mA), 82  $\mu\text{W}$  ( $V_{ds1} = 0.05$  V,  $I_{d1} = 1$  mA, and  $V_{ds2,3} = 0.04$  V,  $I_{d2,3} = 0.8$  mA), 100  $\mu\text{W}$  ( $V_{ds1} = 0.06$  V,  $I_{d1} = 1$  mA, and  $V_{ds2,3} = 0.05$  V,  $I_{d2,3} = 0.8$  mA), 200  $\mu\text{W}$  ( $V_{ds1} = 0.08$  V,  $I_{d1} = 1.5$  mA, and  $V_{ds2,3} = 0.08$  V,  $I_{d2,3} = 1$  mA), 300  $\mu\text{W}$  ( $V_{ds1} = 0.1$  V,  $I_{d1} = 2$  mA, and  $V_{ds2,3} = 0.1$  V,  $I_{d2,3} = 1$  mA) and 600  $\mu\text{W}$  ( $V_{ds1} = 0.2$  V,  $I_{d1} = 2$  mA, and  $V_{ds2,3} = 0.1$  V,  $I_{d2,3} = 2$  mA), respectively.

Fig. 3.7 depicts the input and output P1dB values of the fabricated amplifier. The measured average output P1dB values at 100, 200, and 600  $\mu\text{W}$  dc power are -30.6, -23.2, and -19.1 dBm, respectively. The corresponding average input P1dB values are -53.0, -49.0, and -50.2 dBm, which are sufficient to support more than 2000 qubit readout simultaneously based on analysis in Section 3.1. Notably, even with one-order less dc bias power, the input P1dB of the designed LNA remains comparable to the typically utilized LNA for qubit readout, which is around -52 dBm [26].

In summary, a low-power HEMT LNA has been designed and optimized based on the requirements analysis for its application in the quantum computing readout system. The LNA was a three-stage cascade hybrid design with a suspended transmission line for high-impedance matching required at low power. Based on the measurement results, the LNA successfully achieved its design objectives in terms of noise, power consumption, gain, and dy-

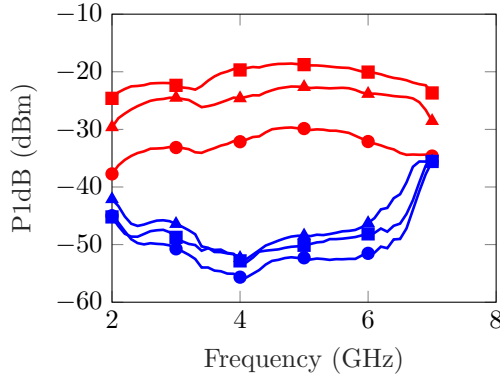


**Figure 3.7:** Measured input and output P1dB of the fabricated LNA circuit at 4 K for various dc power. The blue lines are input P1dB and the red lines are output P1dB. Circle, triangle and square lines represent bias power of 100, 200, and 600  $\mu\text{W}$ , respectively.

dynamic range, aligning with the requirements for qubit readout. The measured noise temperature and gain of the fabricated LNA were found to be in good agreement with simulations, which validated the efficiency of the extracted low-power small-signal noise model for the InP HEMT. The LNA demonstrated qubit readout threshold noise with low power consumption, achieving an  $T_{e,avg}$  of 2.0 K with only 200  $\mu\text{W}$  dc power. To the best of the author's current knowledge, no other semiconductor-based LNA designed for qubit readout frequencies has achieved a 2.0 K noise temperature with power consumption below 2 mW [1], [3], [26]. The significant decrease in dc power consumption and high input P1dB demonstrated by the HEMT LNA in this licentiate thesis highlights the circuit's potential for future large-scale quantum systems.



## CHAPTER 4

---

### A low-power LNA for qubit readout using an optimized InP HEMT

---

In this chapter, the low-power small-signal noise modeling methodology from Chapter 2 will be applied to a novel InP HEMT where the epitaxial structure has been optimized for even lower transistor noise than in Chapter 2. A new InP HEMT model was compared with the standard InP HEMT model derived in Chapter 2. The optimized InP HEMT was tested in the first stage of the low-power 4-6 GHz LNA designed for qubit readout described in Chapter 3. The LNA measurement results were compared with the results in Section 3.3. It will be shown that the optimized InP HEMT can be successfully applied for the LNA in this work to advance state-of-the-art noise performance towards  $100 \mu\text{W}$  dc power consumption. This shows the potential for low-power HEMT LNAs for qubit readout circuitry in future massive quantum computing.

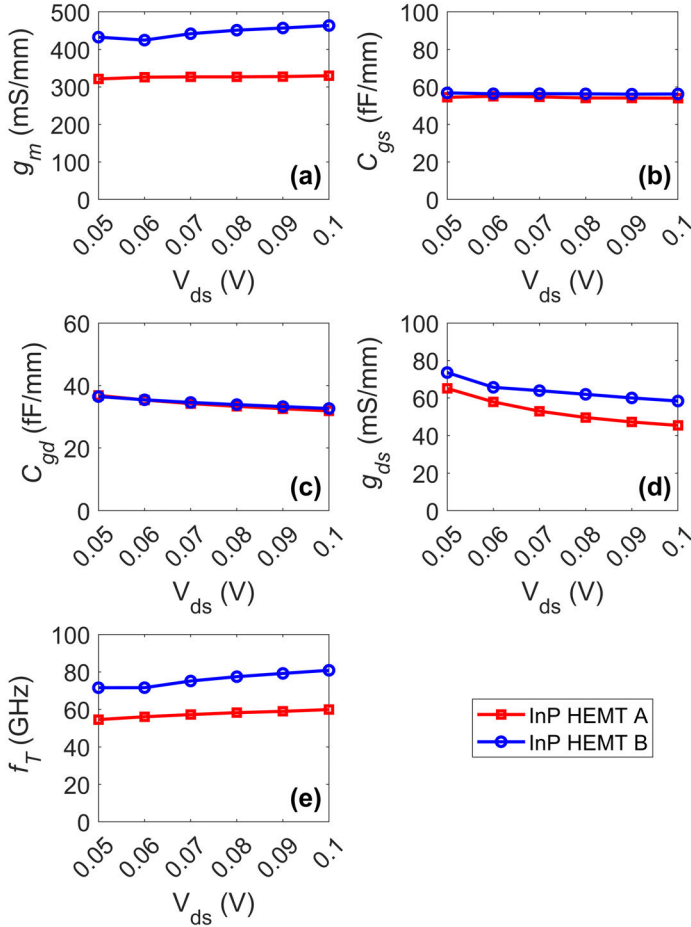
#### 4.1 Optimized HEMT technology for low power

The standard InP HEMT, whose epitaxial structure has been described in Section 2.1, is denoted as HEMT A. The optimized InP HEMT is denoted as

HEMT B. The epitaxial structure of HEMT B is described in [17]. A primary distinction between the HEMTs was small adjustments of the epitaxial layer thickness between gate and channel in the device. Compared to HEMT A, the spacer thickness of HEMT B was changed from 3 to 5 nm and its barrier thickness from 8 to 4 nm. When used in the cryogenic 4-8 GHz hybrid LNA, HEMT A achieved  $T_{e,avg}$  of 1.7 K at a dc power of 12.3 mW. On the other hand, the LNA employing HEMT B exhibited a  $T_{e,avg}$  of 1.4 K while consuming only 6.1 mW dc power [17]. The optimized spacer thickness leads to better channel confinement which shows potential for better noise performance at low power. The quest in this thesis was to evaluate the optimized HEMT B in the model and design approach used for sub-mW LNAs based on HEMT A in Chapter 2 and 3.

## 4.2 Comparison of small-signal noise models

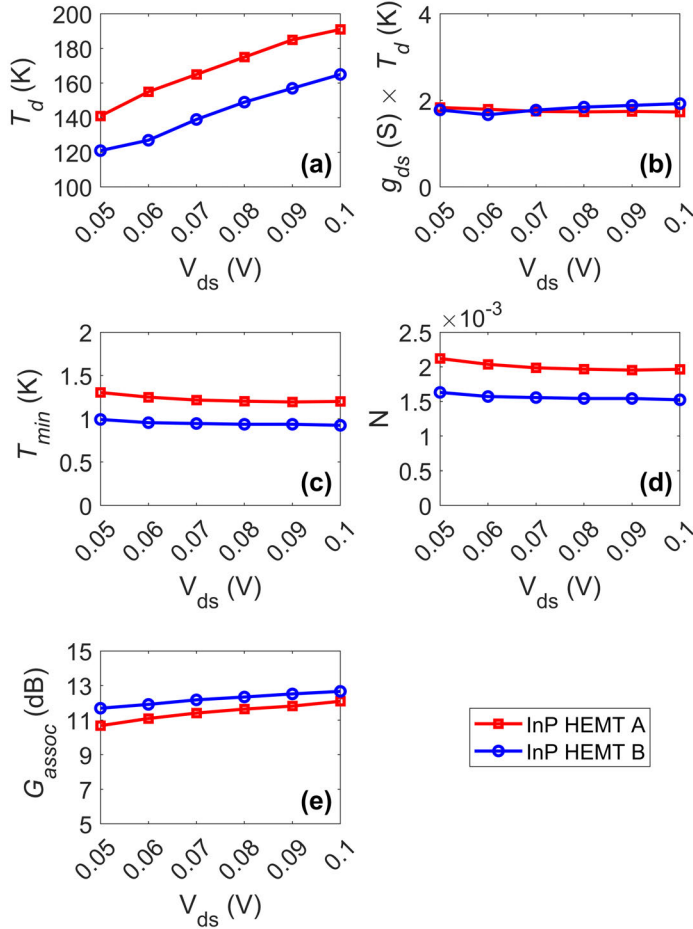
Cryogenic low-power small-signal noise modeling in Chapter 2 has been applied to HEMT B for dc bias points ranging from 0.05 to 0.1V for  $V_{ds}$  and  $I_d = 1$  mA, corresponding to a HEMT bias power of 50 to 100  $\mu$ W. The selected dc bias range was just before the small-signal parameters of HEMT A began to deteriorate rapidly, according to the extracted model in Chapter 2. This chosen bias range allowed for optimizing power consumption while preserving the noise performance of the HEMT. Fig. 4.1 presents the small-signal model parameters for HEMT A and B at 4 K. The small-signal parameters include  $g_m$ ,  $C_{gs}$ ,  $C_{gd}$ ,  $g_{ds}$ , and calculated  $f_T$  as a function of  $V_{ds}$  at an  $I_d$  of 1 mA for both HEMTs. The  $g_m$  of both HEMT A and B remains relatively unaffected by the variation of  $V_{ds}$ . HEMT B's average  $g_m$  is 445 mS/mm, which is 36% higher than HEMT A. Conversely,  $C_{gs}$  and  $C_{gd}$  for both HEMTs are quite similar, as a result of their identical device geometries. The  $C_{gs}$  and  $C_{gd}$  for both HEMTs do not respond to changes in this  $V_{ds}$  interval. In contrast,  $g_{ds}$  of HEMT B is around 20% higher than that of HEMT A. Both HEMTs exhibit a slight increase in  $g_{ds}$  with a decrease in  $V_{ds}$ . The  $f_T$ , taking all small-signal parameters into account, appears to marginally decline when  $V_{ds}$  decreases from 0.1 to 0.05 V.  $f_T$  of HEMT B is 32% higher than HEMT A, primarily due to the difference in  $g_m$ , as indicated by Eq. (2.2). Within the examined low-power range, the small-signal model parameters that exhibit notable differences between HEMT A and B are the channel-related parameters  $g_m$  and



**Figure 4.1:** Small-signal model parameters (a)  $g_m$ , (b)  $C_{gs}$ , (c)  $C_{gd}$ , (d)  $g_{ds}$ , and (e)  $f_T$  as a function of  $V_{ds}$  at 6 GHz for HEMT A and B at 4 K.  $I_d = 1$  mA.

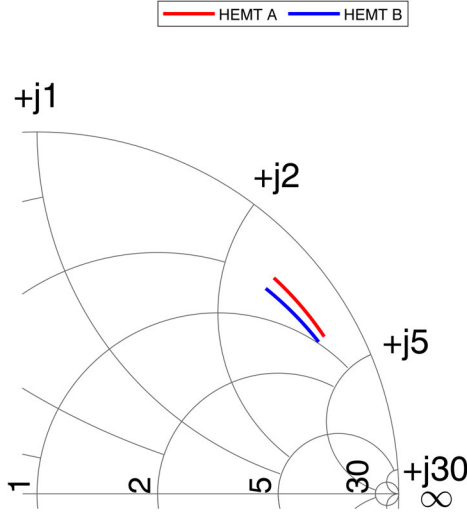
$g_{ds}$ . This distinction can be accounted for by the optimized spacer thickness that leads to better confinement of the two-dimensional electron gas in the cryogenic HEMT channel [17], [35].

Fig. 4.2 illustrates the extracted  $T_d$ , the product of  $g_{ds}$  and  $T_d$ ,  $T_{min}$ ,  $N$ ,



**Figure 4.2:** Noise-model parameters (a)  $T_d$ , (b) product of  $g_{ds}$  and  $T_d$ , (c)  $T_{min}$ , (d)  $N$ , and (e)  $G_{assoc}$  as a function of  $V_{ds}$  at 6 GHz for HEMT A and B at 4 K.  $I_d = 1$  mA.

and  $G_{assoc}$  at 6 GHz as a function of  $V_{ds}$  at an  $I_d$  of 1 mA for both HEMTs at 4 K. As  $V_{ds}$  decreases from 0.1 to 0.05 V,  $T_d$  exhibits a declining pattern, indicating that the channel temperature reduces with less dc power applied. HEMT A has a 10% higher average  $T_d$  compared to HEMT B. Nevertheless,



**Figure 4.3:** The extracted  $\Gamma_{opt}$  from 4 to 6 GHz for HEMT A (red solid line) and B (blue solid line) at 4 K.  $I_d = 1$  mA and  $V_{ds} = 0.05$  V. [From Paper C]

the product of  $T_d$  and  $g_{ds}$  for both HEMTs is quite similar. Consequently, the lower  $T_d$  advantage for HEMT B to reach lower  $T_{min}$  is offset by its increased  $g_{ds}$ . The average  $T_{min}$  for HEMT B is 0.95 K, which is 30% lower than HEMT A (1.23 K). The reduced  $T_{min}$  of HEMT B can therefore be ascribed to its higher  $g_m$  (and effectively  $f_T$ ) values.

In Fig. 4.2 (d), HEMT A appears more sensitive to mismatch than HEMT B, showing a 30% elevated  $N$  value. Due to the variance in  $g_m$ , HEMT B exhibits a slightly higher  $G_{assoc}$  compared to HEMT A, as plotted in Fig. 4.2 (e).

The  $\Gamma_{opt}$  for the noise match at 4-6 GHz for both HEMTs is shown in the Smith chart in Fig.4.3. Relative to HEMT A, HEMT B's  $\Gamma_{opt}$  lies closer to the center of the Smith chart, which is attributed to HEMT B's higher  $g_m$  [28]; See Fig.4.1 (a).

Fig. 4.4 presents the simulated  $T_e$  when matching the input and output of the two HEMT models to  $50 \Omega$  without any matching network at 6 GHz. The  $T_e$  for a  $50 \Omega$  port impedance serves as an initial approximation for the quality of matching, taking all noise model parameters into account. Although the

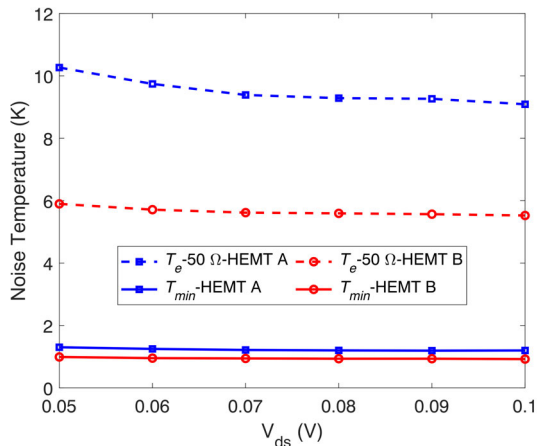


**Figure 4.4:** The simulated  $T_e$  at 6 GHz for HEMT A and B to match both input and output to 50  $\Omega$  situation. The  $T_{min}$  at 6 GHz of both HEMTs are plotted for comparison.  $I_d = 1$  mA. [From Paper C]

average  $T_{min}$  for HEMT A and B differs by only 0.28 K, their average  $T_e$  over  $V_{ds}$  displays a 3.8 K difference. This indicates a more favorable trade-off between noise and bandwidth for HEMT B as opposed to HEMT A when operating at low power.

### 4.3 Measurement results and comparison

The impact from HEMT A or HEMT B on the noise performance at low power is demonstrated using the 4-6 GHz cryogenic LNA designed for qubit readout in this thesis; See Chapter 3. As the initial stage of the LNA is vital in defining overall noise performance, the first stage of the LNA was used to evaluate HEMT A and HEMT B. The performance of LNA A, which employed HEMT A for all three stages, was reported in Section 3.3. LNA B is identical to LNA A but for the first stage where HEMT B replaced HEMT A.

Both LNAs were characterized under 100  $\mu$ W bias ( $V_{d1} = 0.06$  V and  $I_{d1} = 1$  mA, and  $V_{d2,3} = 0.05$  V and  $I_{d2,3} = 0.8$  mA). The corresponding first-stage HEMT bias power was 50  $\mu$ W ( $V_{ds} = 0.05$  V and  $I_d = 1$  mA). As shown in Fig.4.5, the measured  $T_{e,avg}$  for LNA A and LNA B was 2.6 K and 2.0 K,

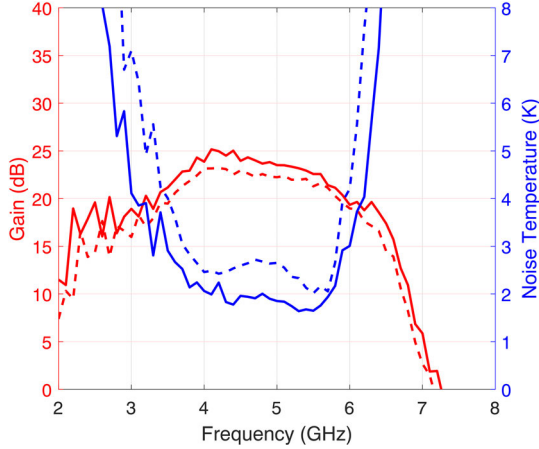


**Figure 4.5:** Measured gain and noise for the 4-6 GHz HEMT LNAs at 4 K under 100  $\mu\text{W}$  dc power consumption. The dashed lines represent LNA A, and the solid lines LNA B. The blue color represents the noise temperature and the red color the gain. [From Paper C]

respectively. The 23% decrease in  $T_{e,avg}$  for LNA B compared to LNA A was mainly due to the increase in  $g_m$  and the reduction in  $T_d$  for HEMT B compared to HEMT A. The average gain for LNA A and LNA B was 22.5 dB and 23.2 dB, respectively. The improved average gain for LNA B compared to LNA A was due to the greater  $G_{assoc}$  of HEMT B compared to HEMT A; See Fig.4.1(b). The measured input P1dB for LNA B was -53 dBm, which was the same as LNA A. The P1dB was mostly limited by the output stage HEMT, which was identical for the two LNAs. The average  $S_{11}$  of LNA B for 4-6 GHz was -7.2 dB, which was 0.9 dB improvement compared to LNA A.

The improved noise performance, gain, and input matching of LNA B compared to LNA A at low power aligns with predictions made by the small-signal noise model comparison in section 4.2. This reinforces that the epitaxially optimized HEMT B, boasting a superior  $g_m$ , offers a more advantageous trade-off between noise performance and bandwidth compared to HEMT A.

## 4.4 State-of-the-art comparison

The performance of LNAs presented in this chapter and Chapter 3 has been compared with state-of-the-art cryogenic amplifiers operating at low dc power in frequency bands targeted for qubit readout, as shown in Table 4.1. A new figure-of-merit (FOM) modified from [20] is proposed where  $T_{e,avg}$  is replaced by  $T_{e,avg,total}$ :

$$FOM = \frac{f_h}{f_l} \times \frac{hf_0}{kT_{e,avg,total}} \times \frac{1}{P_{dc}} \quad (4.1)$$

where

$$T_{e,avg,total} = T_{e,avg} + \frac{T_{e,avg}}{G} + \frac{T_{e,avg}}{G^2} + \frac{T_{e,avg}}{G^3} + \dots = T_{e,avg} \times \frac{G}{G-1} \quad (4.2)$$

and  $f_h$ ,  $f_l$ , and  $f_0$  represent the upper-band, lower-band, and central frequency within the designed bandwidth, respectively;  $P_{dc}$  denotes the total dc power for the LNA;  $G$  is the average gain of LNA. The FOM represent maximum to minimum frequencies scaled by the inverse of both the average number of added photons and the total dc power consumption. The gain is involved by  $T_{e,avg,total}$  that represents the total average noise temperature with infinite number of cascaded LNAs.

Table 4.1 categorizes amplifiers by device technology and ranks them based on their FOM, starting with the highest values. Among the semiconductor-based LNAs, the InP HEMT based LNAs still represent the lowest noise temperature working with minimal dc power consumption, leading to the highest FOM. Although MMIC designs have benefits for mass production, hybrid designs still show better performance. This is due to the design flexibility of the hybrid, especially the ability to use low-loss substrates and other strategies for optimal matching. SiGe HBT-based LNAs are notable for their considerable gain at low power and has the advantage as a silicon technology to be integrated with CMOS. However, the SiGe-HBT LNAs have not achieved top-tier noise performance and is not sufficient on its own for qubit amplification. CMOS LNAs, using refined circuit typologies made possible by mature processes, have been optimized for cryogenic environment and designed for qubit readout. However, compared to InP HEMT and SiGe HBT LNAs, CMOS LNAs exhibit much higher noise and power consumption. Lastly, the TWPA operating at 4 K has below 2.0 K  $T_{e,avg}$  with 100  $\mu$ W dc consumption, which is

**Table 4.1:** Comparison of state-of-the-art cryogenic LNAs for qubit readout frequencies.

Ref.	Amplifier type	Device Technology	Freq. (GHz)	$T_{e,avg}$ (K)	G (dB)	dc power (mW)	FOM ( $10^{-2}mW^{-1}$ )
[22]	MMIC	TWPA	3.5-5.5	1.9	18	100	178.7
[15]	Hybrid	InP HEMT	4-8	4.1	20.0	112	124.2
[15]	Hybrid	InP HEMT	4-8	2.8	27.0	300	68.5
[48]	Hybrid IC	InP HEMT	0.3-14	3.5	41.6	12000	38.1
[14]	Hybrid	InP HEMT	4-8	1.6	44.0	4200	8.57
[35]	Hybrid	InP HEMT	4-8	1.2	42.0	7800	5.7
[49]	Hybrid IC	InP HEMT	4-12	8.1	26	12000	1.2
[50]	MMIC	InP HEMT	4-8	3.8	23.7	770	19.6
[50]	MMIC	InP HEMT	4-8	2.7	31.0	7780	2.7
[49]	MMIC	InP HEMT	4-12	11.6	22	41000	0.2
[51]	MMIC	InP HEMT	4-12	22.5	27	20900	0.2
[52]	Hybrid IC	SiGe HBT	0.1-3	4.6	30.5	1000	48.5
[20]	Hybrid	SiGe HBT	4-8	3.2	27.5	1000	18.0
[19]	Hybrid IC	SiGe HBT	4-8	8.0	30.0	760	9.5
[21]	MMIC	SiGe HBT	3-6	4.3	36.0	1800	5.58
[53]	MMIC	CMOS	6-8	$\approx 39.0$	$\approx 50.0$	4200	0.3
[54]	MMIC	CMOS	4.2-9.2	$\approx 12.7$	$\approx 33.0$	21000	0.3
[55]	MMIC	CMOS	3.9-5.3	10.2	36.5	23100	0.1
<b>This work, LNA B</b>	Hybrid	InP HEMT	4-6	2.0	23.2	100	<b>180.5</b>
<b>This work, LNA A</b>	Hybrid	InP HEMT	4-6	2.6	22.5	100	138.5
<b>This work, LNA A</b>	Hybrid	InP HEMT	4-6	2.0	23.1	200	90.0
<b>This work, LNA A</b>	Hybrid	InP HEMT	4-6	1.6	33.6	600	37.5

a true challenger for InP HEMT cryogenic LNAs. However the TWPA suffers from lower gain and linearity with higher cost and fabrication complexities that restricts its usage.

LNA A in this thesis with 100  $\mu$ W bias power exhibits the highest FOM among the listed semiconductor solutions. It achieves 2.0 K  $T_{e,avg}$  for qubit readout with 200  $\mu$ W bias power. On the other hand, LNA B presented in this study reaches 2.0 K  $T_{e,avg}$  with 100  $\mu$ W bias power. To our knowledge, this represents the most efficient power consumption for a transistor-based LNA achieving 2.0 K threshold noise performance for qubit readout. When benchmarked against the TWPA at 4 K, LNA B has nearly the same noise and dc power consumption with higher gain and linearity. The performance combined with cost-effectiveness, makes the LNA B strong competitor for qubit readout in future large-scale quantum computing system. Furthermore, the next iteration employing optimized InP HEMTs across all LNA stages is

expected to deliver even more superior results.

---

## Conclusions and future work

---

### 5.1 Conclusions

This thesis has developed the HEMT modeling and circuit design methodology for a cryogenic LNA operating below 1 mW. The circuit design targeted the readout of superconducting qubits in a quantum computer. A HEMT LNA consuming 100  $\mu$ W dc power has been demonstrated with 23.2 dB average gain and 2.0 K noise temperature. This represents a new state-of-the-art for qubit readout using semiconductor-based amplification at 4 K.

First, a 100-nm gate-length InP HEMT was characterized for its noise and RF performance at dc biases down to 1  $\mu$ W. A dual-bias strategy ensured accurate noise extraction at low dc bias for the HEMT. The extracted model revealed that  $V_{ds} = 0.05$  V defined a lower limit for maintaining noise performance at reduced power. The model enabled the first-ever design and optimization of an InP HEMT LNA for qubit readout at such low power.

Secondly, the superconducting qubit readout system was discussed regarding its requirement for the HEMT cryogenic LNA. Tailored design goals were set based on the extracted model and application requirements. A suspended transmission line structure was realized in cryogenic vacuum environment to

achieve high impedance for noise match at low-power bias of the InP HEMT. The design method resulted in a 4-6 GHz cryogenic LNA that attained 2.0 K  $T_{e,avg}$  threshold performance for qubit readout with 200  $\mu$ W dc power consumption.

Finally, the 4-6 GHz cryogenic HEMT LNA in Chapter 3 was tested with an InP HEMT slightly modified in the thicknesses of the epitaxial layers. The improvement of model parameters of the new HEMT was analyzed with respect to the standard HEMT. The enhancement in  $g_m$  was the reason for superior noise performance meaning easier matching conditions for the HEMT. The LNA using the optimized InP HEMT as the first stage reached 2.0 K  $T_{e,avg}$  with 100  $\mu$ W bias power, which is a new state-of-the-art performance with even higher FOM than a superconducting TWPA operated at 4 K [22].

## 5.2 Future work

Based on the demonstration of this study, the author believes the following topics can be interesting for future studies:

- **Demonstration of HEMT LNAs with optimized InP HEMT for 6-8 GHz.** The 4-6 GHz LNA employing epi-optimized InP HEMT for the first stage demonstrated large improvement in performance. It is promising to have 6-8 GHz LNA with similar enhanced low-power performance to cover the upper half of commonly used qubit readout frequencies.
- **Test the low-power cryogenic LNA in the qubit readout chain.** It is reported that the qubit can be negatively influenced by the thermal dissipation from the HEMT LNA at 4 K [56]. The low-power cryogenic HEMT LNA with more than one-order power consumption improvement can be tested in the qubit readout chain to further verify this claim. The experiment can pave the way for better integration in qubit readout system.
- **Develop pulsed operation for low-power cryogenic HEMT LNA.** The low-power cryogenic HEMT LNA can be operated under pulse operation due to the pulse nature of qubit readout [5]. A pulsed HEMT LNA can greatly reduce the LNA's average power consumption without sacrificing RF and noise performance. The dynamic response of the

HEMT and LNA needs to be investigated for implementation of pulsed operation of the cryogenic HEMT LNA.

- **High performance InP MMIC LNA.** The developing InP-on-Si technology is promising for fabrication of high-performance and low-power MMICs in much larger volumes than today. The potential to be integrated with CMOS technology will enable more advanced circuit topology to overcome matching difficulties. The MMIC solution can provide larger volumes and higher integration for the whole readout chain.

## **Acknowledgments**

I'd like to express deep gratitude to everyone who supported me and made this work possible.

My heartfelt thanks go to my main supervisor, Professor Jan Grahn, for his support, encouragement, and invaluable discussions throughout this journey.

I'm also thankful to my co-supervisors from Low Noise Factory AB (LNF), Dr. Jörgen Stenarson and Dr. Peter Sobis. Jörgen's guidance in the measurement lab has been invaluable, revealing the true essence of engineering problem-solving. Peter was always supportive, helping me with HFSS and circuit fabrication, and we had many good discussions.

I want to thank Professor Jan Stake, my examiner, for creating a positive scientific atmosphere at the Terahertz and Millimetre Wave Laboratory (TML), and for his consistent encouragement.

A special thank goes to Niklas Wadefalk, CEO of LNF, for enriching my understanding in circuit design, providing access to LNF's resources, and helping polish my manuscripts. Dr. Sumedh Mahashabde and Dr. David Niepce, both from LNF, have inspired me with their expertise in quantum computing. I'm thankful to Johan Embretsén, Production Manager at LNF, for seamlessly coordinating measurements and fabrication timings; and to Hannes Hanhineva, Senior Production Technician at LNF, for helping me assemble the circuits with excellent skills.

I appreciate that Junjie Li for providing me her state-of-the-art InP HEMT. I want to send my regards to Dr. Andrei Vorobiev from TML, for helping me understand semiconductor physics behind my observations, Professor Serguei Cherednichenko for fruitful discussion and helping me many times on the cryogenic probe station, and Dr. Yu Yan for giving me help hand for finding lab components!

I want thank to Hangxi Li from Quantum Technology Laboratory (QTL) for discussing quantum computer architecture with me and invite me to present my work at QTL group meeting, so I can get precious feedback from Professor Per Delsing and Dr. Giovanna Tancredi.

To my friends on the 6th floor of MC2, thanks for your help and the fun times we had. Last but not least, I want to thank my families for your priceless love and support.

This work was supported by the Sweden's innovation agency (Vinnova) in the Strategic Innovation Program Smartare Elektroniksystem and by the

GHz-ChaseOn Bridge Centre at Chalmers University of Technology.



---

## References

---

- [1] J. C. Bardin, D. H. Slichter, and D. J. Reilly, “Microwaves in Quantum Computing,” *IEEE Journal of Microwaves*, vol. 1, no. 1, pp. 403–427, 2021.
- [2] J. Aumentado, “Superconducting parametric amplifiers: The state of the art in Josephson parametric amplifiers,” *IEEE Microwave magazine*, vol. 21, no. 8, pp. 45–59, 2020.
- [3] J. C. Bardin, “Cryogenic Low-Noise Amplifiers: Noise Performance and Power Dissipation,” *IEEE Solid-State Circuits Magazine*, vol. 13, no. 2, pp. 22–35, 2021, ISSN: 1943-0590.
- [4] J. Heinsoo, C. K. Andersen, A. Remm, *et al.*, “Rapid high-fidelity multiplexed readout of superconducting qubits,” *Physical Review Applied*, vol. 10, no. 3, p. 034040, 2018.
- [5] P. Krantz, M. Kjaergaard, F. Yan, T. P. Orlando, S. Gustavsson, and W. D. Oliver, “A quantum engineer’s guide to superconducting qubits,” *Applied Physics Reviews*, vol. 6, no. 2, Jun. 2019, 021318, ISSN: 1931-9401.
- [6] L. Chen, H.-X. Li, Y. Lu, *et al.*, “Transmon qubit readout fidelity at the threshold for quantum error correction without a quantum-limited amplifier,” *npj Quantum Information*, vol. 9, no. 1, p. 26, 2023, ISSN: 2056-6387.

- [7] C. Q. Choi, “IBM’s Quantum Leap: The Company Will Take Quantum Tech Past the 1,000-Qubit Mark in 2023,” *IEEE Spectrum*, vol. 60, no. 1, pp. 46–47, 2023.
- [8] F. Arute, K. Arya, R. Babbush, *et al.*, “Quantum supremacy using a programmable superconducting processor,” *Nature*, vol. 574, no. 7779, pp. 505–510, 2019.
- [9] E. Knill, “Quantum computing with realistically noisy devices,” *Nature*, vol. 434, no. 7029, pp. 39–44, 2005.
- [10] J. C. Bardin, D. Sank, O. Naaman, and E. Jeffrey, “Quantum Computing: An Introduction for Microwave Engineers,” *IEEE Microwave Magazine*, vol. 21, no. 8, pp. 24–44, 2020.
- [11] S. Weinreb, “Low-Noise Cooled GASFET Amplifiers,” *IEEE Transactions on Microwave Theory and Techniques*, vol. 28, no. 10, pp. 1041–1054, 1980.
- [12] T. Mimura, S. Hiyamizu, T. Fujii, and K. Nanbu, “A New Field-Effect Transistor with Selectively Doped GaAs/n- $Al_xGa_{1-x}$ As Heterojunctions,” *Japanese Journal of Applied Physics*, vol. 19, no. 5, p. L225, May 1980.
- [13] T. Mimura, “The early history of the high electron mobility transistor (HEMT),” *IEEE Transactions on Microwave Theory and Techniques*, vol. 50, no. 3, pp. 780–782, 2002.
- [14] J. Schlee, G. Alestig, J. Halonen, *et al.*, “Ultralow-Power Cryogenic InP HEMT With Minimum Noise Temperature of 1 K at 6 GHz,” *IEEE Electron Device Letters*, vol. 33, no. 5, pp. 664–666, 2012, ISSN: 1558-0563.
- [15] E. Cha, N. Wadefalk, G. Moschetti, A. Pourkabirian, J. Stenarson, and J. Grahn, “InP HEMTs for Sub-mW Cryogenic Low-Noise Amplifiers,” *IEEE Electron Device Letters*, vol. 41, no. 7, pp. 1005–1008, 2020.
- [16] E. Cha, N. Wadefalk, G. Moschetti, *et al.*, “Optimization of Channel Structures in InP HEMT Technology for Cryogenic Low-Noise and Low-Power Operation,” *IEEE Transactions on Electron Devices*, pp. 1–6, 2023.

- 
- [17] J. Li, A. Pourkabirian, J. Bergsten, N. Wadefalk, and J. Grahn, “Influence of Spacer Thickness on the Noise Performance in InP HEMTs for Cryogenic LNAs,” *IEEE Electron Device Letters*, vol. 43, no. 7, pp. 1029–1032, 2022.
- [18] J. C. Bardin, “Silicon-germanium heterojunction bipolar transistors for extremely low-noise applications,” Ph.D. dissertation, California Institute of Technology, 2009.
- [19] S. Montazeri, W. T. Wong, A. H. Coskun, and J. C. Bardin, “Ultra-Low-Power Cryogenic SiGe Low-Noise Amplifiers: Theory and Demonstration,” *IEEE Transactions on Microwave Theory and Techniques*, vol. 64, no. 1, pp. 178–187, 2016, ISSN: 1557-9670.
- [20] W. T. Wong, M. Hosseini, H. Rücker, and J. C. Bardin, “A 1 mW Cryogenic LNA Exploiting Optimized SiGe HBTs to Achieve an Average Noise Temperature of 3.2 K from 4–8 GHz,” in *2020 IEEE/MTT-S International Microwave Symposium (IMS)*, pp. 181–184, ISBN: 2576-7216.
- [21] Z. Zou, M. Hosseini, R. Kwende, S. Raman, and J. C. Bardin, “A Frequency and Bandwidth Reconfigurable 3–6 GHz Cryogenic SiGe BiCMOS LNA with a Power Consumption of  $\leq 2.9$  mW,” in *2021 IEEE MTT-S International Microwave Symposium (IMS)*, 2021, pp. 653–656.
- [22] M. Malnou, J. Aumentado, M. Vissers, *et al.*, “Performance of a Kinetic Inductance Traveling-Wave Parametric Amplifier at 4 Kelvin: Toward an Alternative to Semiconductor Amplifiers,” *Physical Review Applied*, vol. 17, no. 4, p. 044009, 2022.
- [23] A. R. Alt and C. R. Bolognesi, “(InP) HEMT Small-Signal Equivalent-Circuit Extraction as a Function of Temperature,” *IEEE Transactions on Microwave Theory and Techniques*, vol. 63, no. 9, pp. 2751–2755, 2015, ISSN: 1557-9670.
- [24] F. Heinz, F. Thome, D. Schwantuschke, A. Leuther, and O. Ambacher, “A Scalable Small-Signal and Noise Model for High-Electron-Mobility Transistors Working Down to Cryogenic Temperatures,” *IEEE Transactions on Microwave Theory and Techniques*, vol. 70, no. 2, pp. 1097–1110, 2022, ISSN: 1557-9670.

- [25] E. Cha, N. Wadefalk, P. Nilsson, *et al.*, “0.3–14 and 16–28 GHz wide-bandwidth cryogenic MMIC low-noise amplifiers,” *IEEE Transactions on Microwave Theory and Techniques*, vol. 66, no. 11, pp. 4860–4869, 2018, ISSN: 0018-9480.
- [26] *LNF4-8C datasheet*, Accessed: 2022-03-08.
- [27] M. W. Pospieszalski, “Extremely low-noise amplification with cryogenic FETs and HFETs: 1970-2004,” *IEEE Microwave Magazine*, vol. 6, no. 3, pp. 62–75, 2005.
- [28] M. Pospieszalski, “Modeling of noise parameters of MESFETs and MODFETs and their frequency and temperature dependence,” *IEEE Transactions on Microwave Theory and Techniques*, vol. 37, no. 9, pp. 1340–1350, 1989.
- [29] L. Barboni, M. Siniscalchi, and B. Sensale-Rodriguez, “TFET-Based Circuit Design Using the Transconductance Generation Efficiency  $g_m/I_d$  Method,” *IEEE Journal of the Electron Devices Society*, vol. 3, no. 3, pp. 208–216, 2015.
- [30] A. Beckers, F. Jazaeri, and C. Enz, “Theoretical limit of low temperature subthreshold swing in field-effect transistors,” *IEEE Electron Device Letters*, vol. 41, no. 2, pp. 276–279, 2020.
- [31] N. Rorsman, M. Garcia, C. Karlsson, and H. Zirath, “Accurate small-signal modeling of HFET’s for millimeter-wave applications,” *IEEE Transactions on Microwave Theory and Techniques*, vol. 44, no. 3, pp. 432–437, 1996.
- [32] P. Tasker and B. Hughes, “Importance of source and drain resistance to the maximum  $f_T$  of millimeter-wave MODFETs,” *IEEE Electron Device Letters*, vol. 10, no. 7, pp. 291–293, 1989.
- [33] J. Schlee, J. Mateos, I. Íñiguez-de-la-Torre, *et al.*, “Phonon black-body radiation limit for heat dissipation in electronics,” *Nature materials*, vol. 14, no. 2, pp. 187–192, 2015.
- [34] E. Cha, N. Wadefalk, G. Moschetti, *et al.*, “Optimization of Channel Structures in InP HEMT Technology for Cryogenic Low-Noise and Low-Power Operation,” *IEEE Trans. Electron Devices*, May 2023.

- 
- [35] E. Cha, N. Wadefalk, G. Moschetti, A. Pourkabirian, J. Stenarson, and J. Grahn, "A 300- $\mu$ W Cryogenic HEMT LNA for Quantum Computing," in *2020 IEEE/MTT-S International Microwave Symposium (IMS)*, pp. 1299–1302, ISBN: 2576-7216.
- [36] J. Schlee, H. Rodilla, N. Wadefalk, P.-Å. Nilsson, and J. Grahn, "Characterization and Modeling of Cryogenic Ultralow-Noise InP HEMTs," *IEEE Transactions on Electron Devices*, vol. 60, no. 1, pp. 206–212, 2013.
- [37] M. W. Pospieszalski, "On the limits of noise performance of field effect transistors," in *2017 IEEE MTT-S International Microwave Symposium (IMS)*, IEEE, pp. 1953–1956, ISBN: 1509063609.
- [38] E. Cha, "InP High Electron Mobility Transistors for Cryogenic Low-noise and Low-power Amplifiers," Ph.D. dissertation, Department of Microtechnology and Nanoscience, Chalmers University of Technology, Sweden, 2020.
- [39] H. Friis, "Noise figures of radio receivers," *Proceedings of the IRE*, vol. 32, no. 7, pp. 419–422, 1944.
- [40] J. Lange, "Noise Characterization of Linear Twoports in Terms of Invariant Parameters," *IEEE Journal of Solid-State Circuits*, vol. 2, no. 2, pp. 37–40, 1967.
- [41] H. A. Haus and R. B. Adler, "Optimum noise performance of linear amplifiers," *Proceedings of the IRE*, vol. 46, no. 8, pp. 1517–1533, 1958.
- [42] J. Heinsoo, C. K. Andersen, A. Remm, *et al.*, "Rapid high-fidelity multiplexed readout of superconducting qubits," *Physical Review Applied*, vol. 10, no. 3, p. 034 040, 2018.
- [43] C. Macklin, K. O'Brien, D. Hover, *et al.*, "A near-quantum-limited Josephson traveling-wave parametric amplifier," *Science*, vol. 350, no. 6258, pp. 307–310, 2015.
- [44] M. Malnou, M. Vissers, J. Wheeler, *et al.*, "Three-wave mixing kinetic inductance traveling-wave amplifier with near-quantum-limited noise performance," *PRX Quantum*, vol. 2, no. 1, p. 010 302, 2021.
- [45] T. White, A. Opremcak, G. Sterling, *et al.*, "Readout of a quantum processor with high dynamic range josephson parametric amplifiers," *Applied Physics Letters*, vol. 122, no. 1, p. 014 001, 2023.

- [46] M. Edwards and J. Sinsky, "A new criterion for linear 2-port stability using a single geometrically derived parameter," *IEEE Transactions on Microwave Theory and Techniques*, vol. 40, no. 12, pp. 2303–2311, 1992.
- [47] J. Fernandez, "A noise-temperature measurement system using a cryogenic attenuator," *TMO progress report*, vol. 15, pp. 42–135, 1998.
- [48] E. Cha, N. Wadefalk, P.-Å. Nilsson, *et al.*, "0.3–14 and 16–28 GHz wide-bandwidth cryogenic MMIC low-noise amplifiers," *IEEE Trans. Microw. Theory Techn.*, vol. 66, no. 11, pp. 4860–4869, Nov. 2018, ISSN: 0018-9480.
- [49] B. Aja, K. Schuster, F. Schafer, *et al.*, "Cryogenic low-noise mHEMT-based MMIC amplifiers for 4–12 GHz band," *IEEE Microwave and wireless components letters*, vol. 21, no. 11, pp. 613–615, 2011.
- [50] F. Heinz, F. Thome, and A. Leuther, "A cryogenic four-channel c-band low-noise amplifier mmic in 50-nm metamorphic high-electron-mobility-transistor technology," in *2023 IEEE/MTT-S International Microwave Symposium - IMS 2023*, 2023, pp. 127–130.
- [51] C.-C. Chiong, W.-J. Tzeng, Y.-J. Hwang, W.-T. Wong, H. Wang, and M.-T. Chen, "Design and measurements of cryogenic MHEMT IF low noise amplifier for radio astronomical receivers," in *2009 European Microwave Integrated Circuits Conference (EuMIC)*, IEEE, 2009, pp. 1–4.
- [52] M. Hosseini and J. C. Bardin, "A 1 mW 0.1-3 GHz Cryogenic SiGe LNA with an Average Noise Temperature of 4.6 K," in *2021 IEEE MTT-S International Microwave Symposium (IMS)*, 2021, pp. 896–899.
- [53] A. Caglar, S. Van Winckel, S. Brebels, P. Wambacq, and J. Craninckx, "Design and Analysis of a 4.2 mW 4 K 6–8 GHz CMOS LNA for Superconducting Qubit Readout," *IEEE Journal of Solid-State Circuits*, 2022.
- [54] B. Lin, H. Mani, P. Marsh, R. Al Hadi, and H. Wang, "A 4.2-9.2 GHz Cryogenic Transformer Feedback Low Noise Amplifier with 4.5 K Noise Temperature and Noise-Power Matching in 22nm CMOS FDSOI," in *2022 IEEE Radio Frequency Integrated Circuits Symposium (RFIC)*, IEEE, 2022, pp. 23–26.

- [55] S. Das, S. Raman, and J. C. Bardin, “Design and Implementation of a 3.9-to-5.3 GHz 65 nm Cryo-CMOS LNA with an Average Noise Temperature of 10.2 K,” in *2022 IEEE/MTT-S International Microwave Symposium-IMS 2022*, IEEE, 2022, pp. 719–722.
- [56] Y. Lu, N. Lambert, A. F. Kockum, *et al.*, “Steady-state heat transport and work with a single artificial atom coupled to a waveguide: Emission without external driving,” *PRX Quantum*, vol. 3, no. 2, p. 020305, 2022.